
11

CHEMICAL DYNAMICS SIMULATIONS OF ENERGY TRANSFER AND UNIMOLECULAR DECOMPOSITION IN COLLISION- INDUCED DISSOCIATION (CID) AND SURFACE-INDUCED DISSOCIATION (SID)

ASIF RAHAMAN AND WILLIAM L. HASE

*Department of Chemistry and Biochemistry
Texas Tech University
Lubbock, TX*

KIHYUNG SONG

*Department of Chemistry
Korea National University of Education
Chongwon, Chungbuk, Korea*

JIANGPING WANG

*Department of Chemistry
Wayne State University
Detroit, MI*

SAMY O. MEROUEH

*Department of Chemistry and Biochemistry
University of Notre Dame
Notre Dame, IN*

- 11.1. Introduction
- 11.2. Methodology of CID and SID Simulations
 - 11.2.1. Potential Energy Functions
 - 11.2.2. Trajectory Initial Conditions
 - 11.2.2.1. CID Simulations
 - 11.2.2.2. SID Simulations
- 11.3. Simulations of CID
 - 11.3.1. Rare-Gas Collisions with Al_6 and Al_{13} Clusters
 - 11.3.1.1. Potential Energy Functions
 - 11.3.1.2. Simulation Results
 - 11.3.1.2.1. CID Cross Sections and $T \rightarrow V$ and $T \rightarrow R$ Energy Transfer
 - 11.3.1.2.2. Comparison of E_0^{CID} and E_0 , the True Dissociation Threshold
 - 11.3.1.2.3. Factors Influencing Energy Transfer in Al_6 CID
 - 11.3.1.3. Qualitative Model for Energy Transfer in CID
 - 11.3.2. Ar Atom Collisions with N-Protonated Glycine and Alanine Polypeptides
 - 11.3.2.1. Potential Energy Functions
 - 11.3.2.2. Simulation Results
 - 11.3.2.2.1. Comparison of Amber and AM1 Peptide Intramolecular Potentials
 - 11.3.2.2.2. Role of the Collision Impact Parameter
 - 11.3.2.2.3. Peptide Size and Collision Energy
 - 11.3.2.2.4. Peptide Structure
 - 11.3.2.2.5. $T \rightarrow V$ versus $T \rightarrow R$ Energy Transfer
 - 11.3.2.2.6. Pathways for Energy Transfer
 - 11.3.2.3. Comparisons with Mahan's Impulsive Energy Transfer Model
- 11.4. Simulations of SID
 - 11.4.1. Potential Energy Surfaces for SID Simulations
 - 11.4.1.1. $\text{Cr}^+(\text{CO})_6$
 - 11.4.1.2. Peptide- H^+
 - 11.4.2. SID Simulation Results
 - 11.4.2.1. Comparison with Experiments
 - 11.4.2.2. Amber and AM1 Models for the Peptide- H^+ Intramolecular Potential
 - 11.4.2.3. Energy Transfer Dynamics
 - 11.4.2.3.1. Pathways for Energy Transfer
 - 11.4.2.3.2. Surface Properties
 - 11.4.2.3.3. Peptide Size, Structure, and Amino Acid Constituents
 - 11.4.2.3.4. Projectile Incident Energy and Angle
 - 11.4.2.3.5. Projectile Orientation and Surface Impact Site
 - 11.4.2.4. Fragmentation Mechanisms
 - 11.4.2.4.1. $\text{Cr}^+(\text{CO})_6$ Dissociation
 - 11.4.2.4.2. Gly- H^+ and Gly₂- H^+ Dissociation
 - 11.4.2.4.3. Peptide- H^+ Shattering in Simulation and Experiments
- 11.5. Future Directions

11.1. INTRODUCTION

Since the early 1960s (Bunker 1962; Blais and Bunker 1962) trajectories, with proper selection of initial conditions, have been used to simulate the dynamics of atomic and molecular collisions, including chemical reactions. The trajectory simulations give an atomic-level description of experiments and provide the type of fundamental information required to develop theoretical models of chemical dynamics. Comparisons between trajectory simulations and both experiments and quantum-dynamics calculations have shown that trajectories often give a correct description of the chemical dynamics (Hase 1998a). For many gas-phase chemical processes classical trajectories give accurate cross sections, rate constants, product energy partitionings, energy transfer probabilities, and other parameters. Quantum effects, contributing to the inaccuracy of classical mechanics, include tunneling through potential energy barriers, transitions between electronic states, and unphysical flow of zero-point energy.

Classical trajectories give accurate results for the energy transfer dynamics associated with collision-induced dissociation (CID) and surface-induced dissociation (SID) (Schultz et al. 1997; Bosio and Hase 1998; Meroueh and Hase 2001; Liu et al. 2003; Martinez-Nuñez et al. 2005). This is expected because of the high collision energy and the large densities of internal states for the projectile ion and surface in CID and SID. In addition, the energy transfer is a direct process, and possible unphysical flow of zero-point energy during the collision is not an important issue. Abrupt, short-time unimolecular dissociation of the projectile, identified as “shattering,” is also expected to be accurately represented by the trajectories (Grebenshchikov et al. 2003). For projectile dissociations that occur on a longer timescale, dissociation may be assisted by flow of zero-point energy into the reaction coordinate, resulting in a unimolecular rate constant that is too large and inaccurate (Hase and Buckowski 1982).

In this chapter the use of classical trajectory chemical dynamics simulations to study energy transfer and unimolecular decomposition in CID and SID are reviewed. The methodology of these simulations is described first. Specific simulations of CID and SID are then reviewed, and important findings of this work with respect to experiment and fundamental theories of chemical dynamics are discussed. The chapter ends with some perspectives of future directions of trajectory simulations of CID and SID.

11.2. METHODOLOGY OF CID AND SID SIMULATIONS

In a classical trajectory study the motions of the individual atoms are simulated by solving the classical equations of motion. For chemical dynamics simulations, these equations have traditionally been expressed in the form of Hamilton's equations (Goldstein 1950)

$$\frac{\partial H}{\partial q_i} = \frac{-dp_i}{dt} \quad \text{and} \quad \frac{\partial H}{\partial p_i} = \frac{dq_i}{dt} \quad (11.1)$$

where H , the sum of the kinetic $T(\mathbf{p}, \mathbf{q})$ and potential energies $V(\mathbf{q})$, is the system's Hamiltonian:

$$H = T(\mathbf{p}, \mathbf{q}) + V(\mathbf{q}) \quad (11.2)$$

In the molecular dynamics community (Schlick 2002) the classical equations have usually been expressed in Newton's form

$$m_i \frac{d^2 q_i}{dt^2} = - \frac{\partial V(\mathbf{q})}{\partial q_i} \quad (11.3)$$

which assume Cartesian coordinates. For the most general case, such as for internal coordinates (Wilson et al. 1955), T depends on both the momenta \mathbf{p} and the coordinates \mathbf{q} . The index i in the equations above is the number of coordinates or conjugate momenta for the Hamiltonian. If Cartesian coordinates are used, this number is $3N$, where N is the number of atoms.

There are several components to a classical trajectory chemical dynamics simulation. A potential energy function $V(\mathbf{q})$ for the system under study must be chosen. An ensemble of trajectories is calculated, with each trajectory specified by the system's initial set of momenta \mathbf{p} and coordinates \mathbf{q} . The initial ensemble of \mathbf{p} and \mathbf{q} is chosen to represent the experiment under investigation or chosen so that a particular dynamical attribute of the system may be studied. Distribution functions are usually sampled randomly in choosing the ensemble of initial conditions, and the methodology of sampling is often called Monte Carlo sampling (Blais and Bunker 1962; Bunker 1962; Peslherbe et al. 1999). An algorithm is required for integrating the classical equations of motion. When the trajectory is completed, the final values of the momenta and coordinates are transformed into properties that may be compared with experiment, such as atomic-level reaction mechanisms, product vibration, rotation, and translation energies, scattering angles, the lifetime of a vibrationally excited molecule, and energies in a molecule's vibrational modes versus time. These components for a classical trajectory simulation are incorporated in the general chemical dynamics program VENUS. The Cartesian coordinate representation is the most general for systems of any size, and VENUS uses Cartesians.

Detailed descriptions have been given previously of the abovementioned components for a classical trajectory simulation (Sun and Hase 2003; Bolton et al. 1998; Hase 1998b,c; Peslherbe, et al. 1999; Bolton and Hase 1998). In the following section a brief description of these components is given, as applied to CID and SID.

11.2.1. Potential Energy Functions

The potential energy function used for the SID simulations is written as

$$V = V_{\text{projectile}} + V_{\text{surface}} + V_{\text{projectile, surface}} \quad (11.4)$$

where $V_{\text{projectile}}$ is the projectile's intramolecular potential, V_{surface} is the surface potential, and $V_{\text{projectile, surface}}$ is the projectile–surface intermolecular potential. For CID the potential used is

$$V = V_{\text{projectile}} + V_{\text{projectile, Rg}} \quad (11.5)$$

where Rg represents a rare-gas atom.

Equation (11.4) is an approximation for the exact SID potential. Although the potential describes projectile dissociation on impact with the surface, possible reaction(s) of the projectile with the surface are not included. Also, a fixed set of parameters is used for the $V_{\text{projectile, surface}}$ intermolecular potential. If the structures of the projectile and/or surface change, the charge distribution on the atoms may change, which may affect the intermolecular parameters. Such changes in the intermolecular potential are not included in this potential model with fixed parameters. There is the same limitation for $V_{\text{projectile, Rg}}$ in Eq. (11.5). The models represented by Eqs. (11.4) and (11.5) are expected to give correct energy transfer results and projectile dynamics for direct impulsive collisions, when the projectile and surface have structures for which the intermolecular parameters were obtained. This is the manner in which the simulations were performed and, as is seen below where the simulation results are discussed, excellent agreement is obtained with many features of the experiments.

If the projectile sticks to the surface or the rare gas, and its conformation changes, the nature of the intermolecular potential may also change. The best way to model these types of collisions is by a direct dynamics quantum-mechanical (QM) calculation for a Rg + projectile system (Liu et al. 2003) and a quantum-mechanical/molecular mechanical (QM/MM) calculation for a projectile + surface system (Li et al. 2000). In these methods the QM theory will directly provide the intermolecular potential and represent any changes in its form.

V_{surface} is an analytic function with parameters so that properties of the surface agree with those from experiment. The $V_{\text{projectile, surface}}$ intermolecular potential is a sum of two-body potentials between the atoms of the projectile and those of the surface, and $V_{\text{projectile, Rg}}$ is a sum of two-body potentials between the Rg atom and atoms of the projectile.

Both analytic and electronic structure theory models were used for the projectile's potential energy function, $V_{\text{projectile}}$. The analytic potential models used for the Al_n and $\text{Cr}^+(\text{CO})_6$ clusters properly describe their dissociations. On the other hand, the analytic potentials used for protonated peptides are molecular mechanics (MM) quadratic forcefield and nonbonded potential models, and dissociation pathways are not represented. To study the dissociation dynamics of peptide ions, the AM1 semiempirical QM electronic structure theory model was used for the peptide's potential. The classical trajectory chemical dynamics with AM1 are QM+MM direct dynamics simulations (Sun and Hase 2003; Hase et al. 2003), with MM-type analytic functions for the remaining potential energy terms. Details of the specific models used for $V(\mathbf{q})$ are described below as part of the simulation results. More accurate QM theories such as DFT or MP2 may be used for peptides with one

or two amino acids. However, the use of such higher-level theories are not computationally practical for large peptides. For these peptides, a semiempirical method with a floating-occupation molecular orbital configuration interaction wavefunction (Granucci and Toniolo 2000) may be practical and sufficiently accurate QM method.

11.2.2. Trajectory Initial Conditions

11.2.2.1. CID Simulations. To choose initial conditions for a trajectory representing the collision of a rare-gas atom with a polyatomic ion involves first randomly sampling the coordinates and momenta of the ion and then selecting random conditions for the relative properties between the atom and polyatomic ion collision partners. In experiments, the polyatomic ion is prepared at a temperature T . To simulate this condition, the quasiclassical method (Truhlar and Muckerman 1979) is used to randomly sample the ion's rotational and vibrational energy levels and then transform them to the Cartesian coordinates and momenta used for the trajectory. The following are the specific steps performed for this sampling procedure:

1. The normal-mode frequencies $\omega = 2\pi\nu$ and normal-mode eigenvector \mathbf{L} for the polyatomic ion are determined by diagonalizing its mass weighted Cartesian force constant matrix (Califano 1976).
2. The harmonic oscillator QM Boltzmann distribution

$$P(n_i) \propto \exp\left[-\left(n_i + \frac{1}{2}\right)h\nu_i/kT\right] \quad (11.6)$$

is randomly sampled for each of the ion's normal modes to select its vibrational quantum number n_i . The energy for the normal mode is

$$E_i = \left(n_i + \frac{1}{2}\right)h\nu_i.$$

3. The polyatomic ion is assumed to be a symmetric top (i.e., this approach is also accurate for spherical tops, but approximate for asymmetric tops) and its angular momentum j and component j_z along the z axis are found by sampling their classical Boltzmann distributions (Bunker and Goring-Simpson 1973). The resulting projection of j into the xy plane [i.e., $(j^2 - j_z^2)^{1/2}$] is randomly assigned onto the x and y axes. The random values of j_x, j_y, j_z , form the rotational angular momentum vector \mathbf{j} for the polyatomic ion.
4. The energy for each normal mode, selected in step 1, is expressed classically as

$$E_i = \frac{P_i^2 + \omega_i^2 Q_i^2}{2} \quad (11.7)$$

where the P_i and Q_i are the normal-mode momenta and coordinates. Random values for P_i and Q_i , with energy E_i , are chosen by giving each normal mode a

random phase. This gives random \mathbf{Q} and \mathbf{P} for the normal modes. The total energy for the polyatomic ion E° is a sum of its vibration and rotation energies, i.e.

$$E^\circ = \sum_{i=1}^{3N-6} E_i + 3RT/2 \quad (11.8)$$

5. The \mathbf{Q} and \mathbf{P} are transformed to Cartesian coordinates \mathbf{q} and momenta \mathbf{p} for the polyatomic ion's N atoms using the normal-mode eigenvector \mathbf{L} (Califano 1976):

$$\mathbf{q} = \mathbf{q}_0 + \mathbf{M}^{(-1/2)} \mathbf{L} \mathbf{Q} \quad (11.9a)$$

$$\mathbf{p} = \mathbf{M}^{1/2} \mathbf{L} \mathbf{P} \quad (11.9b)$$

where \mathbf{q}_0 is a matrix of equilibrium coordinates and \mathbf{M} is the diagonal matrix whose elements are the atomic masses.

6. Since normal modes are approximate for finite displacements (Califano 1976), a spurious angular momentum \mathbf{j}_s arises following this transformation (Chapman and Bunker 1975; Sloane and Hase 1977). The spurious momentum is found from

$$\mathbf{j}_s = \sum_{i=1}^N \mathbf{r}_i \times m_i \dot{\mathbf{r}}_i \quad (11.10)$$

where m_i is the mass of the i th atom and \mathbf{r}_i is its position vector. The desired angular momentum \mathbf{j} is added to the molecule by forming the vector

$$\mathbf{j}_a = \mathbf{j} - \mathbf{j}_s \quad (11.11)$$

and adding the rotational velocity $\boldsymbol{\omega} \times \mathbf{r}_i$ to each of the atoms, where

$$\boldsymbol{\omega} = \mathbf{I}^{-1} \mathbf{j}_a \quad (11.12)$$

and \mathbf{I}^{-1} is the inverse of the inertia tensor (Goldstein 1950).

7. The actual internal energy E for the Cartesian coordinates and momenta, chosen from steps 1–6, is calculated using the correct Hamiltonian and compared with the intended energy E° . If they do not agree within some acceptance criterion, the Cartesian coordinates and momenta are scaled by $(E^\circ/E)^{1/2}$. Any spurious center of mass translational energy is subtracted from the molecule, and the procedure loops back to step 6. If E is within the acceptance criterion of E° , the selected coordinates \mathbf{q} and momenta \mathbf{p} of the polyatomic ion are saved.

The following steps are carried out to choose relative properties between the polyatomic ion and rare-gas atom:

8. To study energy transfer for ion dissociation, random collision impact parameter b is chosen between 0 and b_{\max} , where b_{\max} is the largest impact parameter leading to energy transfer in excess of the ion's dissociation threshold. b_{\max} is determined by tests. An approximate way to choose b_{\max} is to assume a value for the collision cross section, πb_{\max}^2 .
9. The polyatomic ion's Cartesian coordinates and momenta, selected above, are randomly rotated through Euler's angles (Wilson et al. 1955) to give a random orientation

$$\mathbf{q} = \text{ROT}(\theta, \phi, \chi)\mathbf{q} \quad \dot{\mathbf{q}} = \text{ROT}(\theta, \phi, \chi)\dot{\mathbf{q}} \quad (11.13)$$

where $\text{ROT}(\theta, \phi, \chi)$ is the Euler rotation matrix (Wilson et al. 1955).

10. Since the polyatomic ion A has a random orientation in a space-fixed coordinate frame, the B atom may be placed in the y,z plane without loss of generality. The x,y,z coordinates of B are then

$$x = 0 \quad y = 0 \quad z = (s^2 - b^2)^{1/2} \quad (11.14)$$

where s is the initial separation between B and the A center of mass and b is the impact parameter.

11. The A + B relative velocity v_{rel} is now added along the z axis with the restraint that the A + B center of mass remains at rest. The space-fixed Cartesian momenta are then

$$\mathbf{p} = \mathbf{M}(\dot{\mathbf{q}} - \dot{\mathbf{q}}_{\text{rel}}) \quad (11.15)$$

The elements of the relative velocity $\dot{\mathbf{q}}_{\text{rel}}$ are zero for the x and y components and equal to $[m_A/(m_A + m_B)]v_{\text{rel}}$ for the z component of atom B, and equal to $-[m_A/(m_A + m_B)]v_{\text{rel}}$ for the z component of each atom of A.

This concludes the section on random Cartesian coordinates and momenta for a CID trajectory.

11.2.2.2. SID Simulations. For a SID trajectory, initial conditions are chosen for the polyatomic projectile ion, the surface, and relative properties for the projectile-surface collision. Random Cartesian coordinates and momenta are chosen for the projectile ion as described by steps 1–7 and 9 above.

Harmonic quasiclassical (Bosio and Hase 1997), harmonic classical (Song et al. 1995), and anharmonic classical (Meroueh and Hase 2001) approaches have been used to choose random coordinates and momenta for the surface at temperature T_s . Since zero-point energy is added to the surface in the quasiclassical method, the total energy added to the surface is substantially larger for this initial condition sampling

approach as compared to either the harmonic or anharmonic classical sampling. Tests of possible effects of this different surface energy for energy transfer in gas–surface collisions has been investigated in collisions of rare-gas atoms with alkyl thiolate self-assembled monolayer (SAM) surfaces at much lower collision energies (Yan and Hase 2002) than those for SID. Within the statistical uncertainties of these simulations, the quasi-classical harmonic and classical anharmonic sampling methods give the same energy transfer efficiencies. The effect of zero-point energy and classical versus quantum T_s is expected to be even less important for the high collision energies of SID. Each of these sampling methods is discussed below, and classical anharmonic sampling is preferred since all potential energy minima and structures are sampled in this approach.

If the model for the surface is sufficiently small, a normal-mode analysis, as described in step 1 above, may be performed to determine the vibrational frequencies and eigenvectors for the surface normal modes of vibration (i.e., phonons). For quasiclassical sampling of the surface's coordinates and momenta at T_s , the above steps 1–7 are performed with the surface's rotational angular momentum \mathbf{j} set to zero. This quasiclassical approach samples a QM temperature for T_s , since Eq. (11.6) is used to sample the quantum numbers for the surface's vibrational modes. To sample a classical T_s temperature for the surface, the energy for each surface mode is randomly selected according to the classical statistical mechanical distribution function

$$P(E_i) = \exp(-E_i/RT_s)/RT_s \quad (11.16)$$

which gives an average mode energy of RT_s . Initial coordinates and momenta are then chosen for the surface, using steps 1–7 above with the preceding classical mechanical algorithm replacing step 2.

The classical mechanical sampling method described above assumes the molecule vibrates about its potential energy minimum with harmonic frequencies. This model is accurate for a surface, such as diamond, with a single potential energy minimum populated at the temperature T_s and whose frequencies are accurately approximated by the harmonic oscillator model. However, for many surfaces, which have soft forces (i.e., low frequencies) and multiple potential energy minima, this model is inappropriate. Liquid and solid hydrocarbon and self-assembled monolayer (SAM) surfaces fall into this class. Classical initial conditions for such surfaces may be selected by performing a standard molecular dynamics (MD) simulation (Allen and Tildesley 1987), which samples the surface's anharmonic potential. Initial random velocities are chosen for the surface atoms by sampling each atom's Maxwell–Boltzmann distribution at T_s . The surface is then equilibrated by a MD trajectory simulation, with velocity rescaling, so there is equilibration between the surface's kinetic and potential energies for T_s resulting in random \mathbf{p} and \mathbf{q} for the surface.

The remaining step in the sampling for SID is to choose the relative properties for the projectile–surface collisions. The projectiles collide with a collision energy E_i and incident angle θ_i . Their impact points with the surface are random. Two approaches have been used to sample random relative properties for the projectile surface collisions. For one (Bosio and Hase 1997), a beam of projectiles, as illustrated in Figure 11.1, is directed toward the surface as in a SID experiment. The

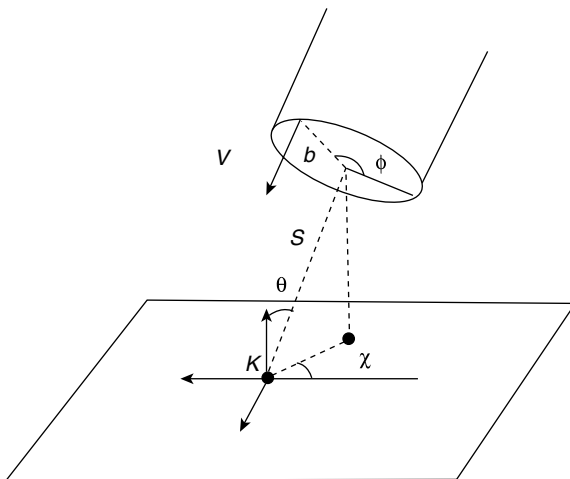


FIGURE 11.1. Definition of coordinates used to sample initial conditions for a SID simulation. [Reprinted with permission from Bosio and Hase (1997).]

projectile ions are randomly placed in a circular area of the beam, with radius r , so that the area spanned by the beam overlaps a unit area on the surface. A projectile is placed randomly in the beam by choosing a random value of b between 0 and b_{\max} (see step 8 above for CID simulations) and a random value for the ϕ angle between 0 and 2π . Then incident angle θ_i is fixed and the center of the beam of projectiles is aimed at the middle of the surface's center unit cell (i.e., the aiming point K). The distance S is between the center of the beam and the aiming point K . A shortcoming of this approach is that a single unit cell on the surface is not sampled uniformly.

In experiments, there are often different domains of growth on the surface and each domain may have a different orientation with respect to the beam of projectiles. This orientation is identified by the azimuthal angle χ in Figure 11.1. If it were possible to scatter projectiles off individual domains of growth, for which the orientation is known, it would be possible to perform experiments with χ selected. On the other hand, if the domains on which the projectiles collide is not controlled, there is probably a random distribution of χ for the projectile–surface collisions. To model this latter experimental condition, χ is randomly chosen from a uniform distribution between 0 and 2π .

In a second approach for choosing properties of the projectile–surface collisions, projectiles with E_i and θ_i are randomly aimed at points within the central unit cell of the surface, which provides uniform sampling of impact sites in the unit cell. As described above, the collisions may have either a fixed or a random azimuthal angle χ . Some experiments are performed with large domains of regular, periodic structures on the surface, with a well-defined unit cell (Isa et al. 2004). This is an excellent method for modeling such systems. It should be noted that simulations of peptide- H^+ SID have shown that the energy transfer dynamics is insensitive to the surface site impacted by the center of mass of the peptide ion (Rahaman et al.

2006). Such a result is not unexpected given the size of a peptide ion and the multiple surface sites its atoms strike. Thus, for simulations of peptide-H⁺ SID, periodic surface models may be adequate for representing experimental surfaces that may be rough at the molecular level.

11.3. SIMULATIONS OF CID

Classical trajectory simulations of the CID of Al₆ and Al₁₃ clusters (de Sainte Claire et al. 1995; de Sainte Claire and Hase 1996) and of protonated polyglycine and polyalanine (Meroueh and Hase 1999, 2000) and Cr⁺(CO)₆ (Martinez-Nuñez et al. 2005) have provided an atomic-level description of the dynamics of energy transfer in CID and the ensuing unimolecular fragmentation. The simulations have shown how the CID dynamics depend on the structure and vibrational frequencies (i.e., stiffness) of the cluster, the mass of the collision partner, repulsiveness of the intermolecular potential between the cluster and collision partners, and the collision's relative velocity. The simulations are based on accurate intermolecular potentials derived from high-level ab initio calculations. Large collision energies were considered in the simulations, and thus it is the short-range region of the intermolecular potential that is important for the CID dynamics. Obtaining this part of the potential accurately, from ab initio calculations, is much less challenging than determining the attractive potential and its energy minimum, since electron correlation is much less important for the repulsive component as compared to the attractive component. Both analytic functions and electronic structure methods were used to represent the intramolecular potential energy functions of the clusters. In the following these simulations are reviewed and a number of important findings obtained from these simulations are discussed.

11.3.1. Rare-Gas Collisions with Al₆ and Al₁₃ Clusters

Chemical dynamics simulations of aluminum cluster CID (de Sainte Claire and Hase 1996; de Sainte Claire et al. 1995) are discussed below.

11.3.1.1. Potential Energy Functions. Two different Al₆ analytic potential energy functions were used in CID. One consists of two-body Lennard-Jones (L-J) terms

$$V_{ij} = \frac{A}{r_{ij}^{12}} + \frac{B}{r_{ij}^6} \quad (11.17)$$

and three-body Axilrod–Teller (A-T) terms

$$V_{ijk} = C \frac{1 + 3 \cos \alpha_1 \cos \alpha_2 \cos \alpha_3}{(r_{ij} r_{jk} r_{ki})^3} \quad (11.18)$$

with parameters $A = 2,975,343.77 \text{ kcal} \cdot \text{\AA}^{12}/\text{mol}$, $B = -17,765.823 \text{ kcal} \cdot \text{\AA}^6/\text{mol}$, and $C = 81,286.093 \text{ kcal} \cdot \text{\AA}^9/\text{mol}$ determined by a fit to ab initio calculations for Al_n ($n = 2-6, 13$) clusters (Petterson et al. 1987). The r_{ij} , r_{jk} , r_{ki} and $\alpha_1, \alpha_2, \alpha_3$ in Eq. (11.18) represent the sides and angles, respectively, of the triangle formed by the three particles i , j , and k .

The second Al_6 analytic function consists of two-body Morse terms with the exponential β parameter written as a cubic function of r_{ij} (Hase et al. 1987), that is

$$V_{ij} = D_e \{1 - \exp[-\beta(r_{ij} - r_e)]\}^2 - D_e \quad (11.19a)$$

$$\beta = \beta_e + c_2 \Delta r^2 + c_3 \Delta r^3 \quad (11.19b)$$

where $\Delta r = r_{ij} - r_e$. Parameters in this Morse function were varied to determine how “stiffness” of the Al_6 cluster affects energy transfer. The octahedral (O_h) Al_6 cluster was used for this study. Parameters for the Morse potentials, identified as Morse^{*} n and Morse/ n , were chosen so that they give the same equilibrium geometry and dissociation energy for Al_6 (O_h) as the L-J/A-T potential presented above but give vibrational frequencies for Al_6 (O_h) that are n times larger and smaller, respectively, than those of the L-J/A-T potential. The L-J/A-T potential of Eqs. (11.17) and (11.18), with the parameters given above, was used to represent the potential energy surface for the different Al_{13} clusters.

Equations (11.17) and (11.18) give multiple potential energy minima for Al_6 and Al_{13} , with a wide variety of structures. The structures considered in the simulations are shown in Figure 11.2. They are octahedral O_h and planar C_{2h} for Al_6 , and D_{3d} [face-centered cubic (fcc)] and planar D_{2h} and D_{6h} for Al_{13} . The threshold energies for dissociation of these clusters to $\text{Al}_5 + \text{Al}$ and to $\text{Al}_{12} + \text{Al}$ are as follows: Al_6 (C_{2h}), 43.8 kcal/mol; Al_6 (O_h), 38.8 kcal/mol; Al_{13} (D_{2h}), 57.5 kcal/mol; Al_{13} (D_{6h}), 42.3 kcal/mol; and D_{3d} (fcc), 16.8 kcal/mol.

Intermolecular potentials for Ne, Ar, and Xe rare-gas (Rg) atom collisions with Al_6 and Al_{13} were written as a sum of two-body potentials between the Rg and Al atoms. Both Rg–Al and Rg– Al^+ potentials were calculated using unrestricted MP2 theory (Head-Gordon et al. 1988; Frisch et al. 1988) with the 6-31G^{*} basis set (Hariharan and Pople 1973, 1974). At long range the Rg– Al^+ potential is more attractive than that for Rg–Al because of the former’s ion-induced dipole interaction. However, for the high translational energies of CID, it is the short-range potential that is important, and Rg–Al and Rg– Al^+ have similar short-range potentials. Also, the positive charge is delocalized for the Al_n^+ cluster and, as a result, the Rg–Al two-body potential for this cluster should be intermediate of those for Rg–Al and Rg– Al^+ . For the energies of CID, Rg– Al_n and Rg– Al_n^+ are expected to have similar intermolecular potentials.

A very accurate fit to the Ar–Al potential is obtained with

$$V = \frac{a}{r^{12}} + \frac{b}{r^6} + c \exp(-dr) \quad (11.20)$$

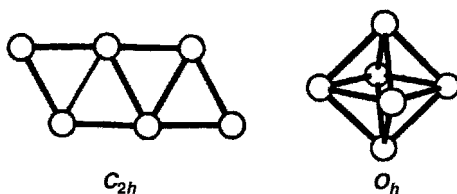
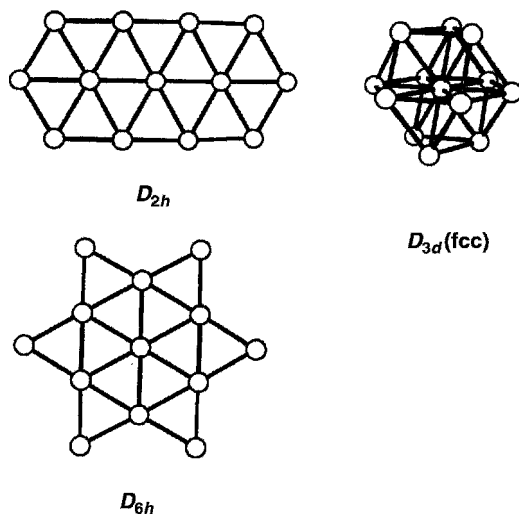
Al₆ minima structures**Al₁₃ minima structures**

FIGURE 11.2. Al₆ and Al₁₃ structures modeled in the CID simulations. [Adapted with permission from de Sainte Claire et al. (1995).]

where r is the distance between Ar and the Al atom. The parameters in this equation are $a = 5212.13281 \text{ kcal} \cdot \text{\AA}^{12}/\text{mol}$, $b = 884.959534 \text{ kcal} \cdot \text{\AA}^6/\text{mol}$, $c = 10,421.443 \text{ kcal/mol}$, and $d = 2.75301790 \text{ \AA}^{-1}$. The short-range repulsive regions of the Rg–Al potentials are accurately described by

$$V = V_0 \exp\left(\frac{-r}{L}\right) \quad (11.21)$$

where L is the range parameter for the intermolecular interaction. The Ne–Al, Ar–Al, and Xe–Al potentials were fit with Eq. (11.21), and the V_0 and L parameters are $V_0 = 17642.938 \text{ kcal/mol}$ and $L = 0.2819 \text{ \AA}$ for Ne, $V_0 = 17352.530 \text{ kcal/mol}$ and $L = 0.3503 \text{ \AA}$ for Ar, and $V_0 = 18479.848 \text{ kcal/mol}$ and $L = 0.4019 \text{ \AA}$ for Xe.

11.3.1.2. Simulation Results. Initial conditions were chosen for the trajectories to represent CID experiments (Jarrold et al. 1987; Hanley et al. 1987). A 138 K rotation

energy of $RT/2$ was added to each principal axis of the cluster, to give a total initial cluster rotational energy E_{rot} of 0.4 kcal/mol. A test showed that the CID cross section and energy transfer distribution for $\text{Ar} + \text{Al}_6(O_h)$ are insensitive to whether the zero-point energy of 4.1 kcal/mol is added to Al_6 in the initial conditions (de Sainte Claire et al. 1995). As a result of this test, initially vibrationless Al_n clusters were considered for all the simulations.

11.3.1.2.1. CID Cross Sections and $T \rightarrow V$ and $T \rightarrow R$ Energy Transfer. The final cluster internal energy was evaluated for each trajectory, and the difference between the final and initial cluster energies is denoted ΔE_{int} . The cluster is assumed to have sufficient energy to dissociate if its final internal energy is larger than its dissociation threshold, which is the assumption of RRKM unimolecular rate theory (Baer and Hase 1996). Cross sections were calculated as a function of collision energy E_{rel} and fit by

$$\sigma_{\text{CID}} = A(E_{\text{rel}} + E_{\text{rot}} - E_0^{\text{CID}})^n / E_{\text{rel}} \quad (11.22)$$

Similar CID cross sections were found for $\text{Al}_6(O_h)$ and $\text{Al}_6(C_{2h})$. For example, at E_{rel} of 120.8 kcal/mol σ_{CID} is 21.7 and 22.8 Å² for $\text{Al}_6(O_h)$ and $\text{Al}_6(C_{2h})$, respectively. Their σ_{CID} fitted parameters for Eq. (11.22) are $A = 40.0 \text{ Å}^2$, $E_0^{\text{CID}} = 52.7 \text{ kcal/mol}$, and $n = 0.99$ for $\text{Al}_6(O_h)$, and for $\text{Al}_6(C_{2h})$, $A = 44.6 \text{ Å}^2$, $E_0^{\text{CID}} = 54.9 \text{ kcal/mol}$, and $n = 0.98$. For $n = 1$, Eq. (11.22) reduces to the well-known hard-sphere model, in which the effective energy is directed along the line of centers and the parameter A equals πb_{max}^2 . That the fitted value of n is near unity indicates a hard-sphere and line-of-centers energy transfer model adequately describes both $\text{Al}_6(O_h)$ and $\text{Al}_6(C_{2h})$. By assuming this model, a b_{max} value of 3.6 Å is extracted from the A parameter for $\text{Al}_6(O_h)$, which is in agreement with the b_{max} values determined directly from the trajectories.

The similar cross sections for $\text{Al}_6(O_h)$ and $\text{Al}_6(C_{2h})$ arise from different attributes of the collision. The planar cluster has b_{max} of 5.5 Å, that is, 2.0 Å larger than that for the octahedral cluster. Also for $b \leq b_{\text{max}}$ a larger fraction of the trajectories for the planar cluster do not transfer sufficient energy for CID to occur. These two effects combine to give similar CID cross sections for the two clusters. The b_{max} value of 3.8 Å extracted from the A parameter for $\text{Al}_6(C_{2h})$ is considerably smaller than $b_{\text{max}} = 5.5 \text{ Å}$ for the trajectories. Trajectories with relatively small impact parameters do not collide with the planar C_{2h} cluster, if the collision's relative velocity is parallel to the cluster's surface plane.

Energy transfer distribution functions for the planar and octahedral Al_6 clusters are compared in Figure 11.3. For both clusters there are no trajectories which transfer all of E_{rel} (i.e., 120.8 kcal/mol) to cluster internal energy. The two distribution functions are quite different, with the increase in the energy transfer probability from zero at large ΔE_{int} much more pronounced for the octahedral cluster. Most of the energy transfer to the $\text{Al}_6(O_h)$ cluster is in the form of vibration. For $E_{\text{rel}} = 120.8 \text{ kcal/mol}$, the average energy transfer to cluster vibration is 35.5 kcal/mol. The average energy transfer to rotation is much lower: only

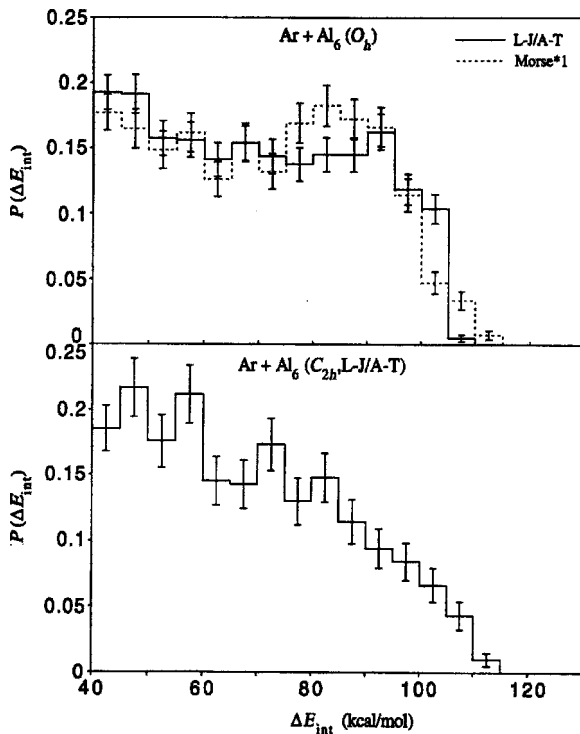


FIGURE 11.3. Ar + Al₆ energy transfer distributions for $E_{\text{rel}} = 120.8$ kcal/mol. $P(\Delta E_{\text{int}})$ is in units of $(\text{kcal/mol})^{-1}$, and the distributions are normalized so that the total probability is unity for transferring energy in excess of the true dissociation threshold E_0 . The probabilities on the y axis have been multiplied by a factor of 10. [Reprinted with permission from de Sainte Claire et al. (1995).]

4.8 kcal/mol. Unfortunately, the distinction between transfer to vibration and rotation was not determined for Al₆(C_{2h}), but because of its planar structure transfer to rotation is expected to be significant (see discussion below).

CID cross sections were calculated for the D_{3d} (fcc), D_{6h} , and D_{2h} Al₁₃ clusters at $E_{\text{rel}} = 120.8$ kcal/mol and a cluster rotational temperature T_{rot} of 138 K. The dissociation threshold of the spherical-type D_{3d} (fcc) cluster is substantially smaller than those of the planar D_{2h} and D_{6h} clusters (see numbers above). The former cluster is compact and has a b_{max} for CID equal to 5.0 Å, while b_{max} is 6.5 Å for the planar less compact clusters. The CID cross sections calculated from the trajectories are 54.7, 47.7, and 35.4 Å², and the fraction of the trajectories that transfer sufficient energy for CID to occur is 0.70, 0.36, and 0.27 for the D_{3d} (fcc), D_{6h} , and D_{2h} clusters, respectively. These latter fractions are consistent with the different dissociation thresholds for the clusters.

For the planar D_{2h} and D_{6h} clusters a large fraction, 39% and 35%, respectively, of the energy transfer is to rotation. For the spherical D_{3d} , the fraction is much smaller and only 7%. Larger rotational energy transfer is expected for D_{2h} and D_{6h}

clusters in comparison to the D_{3d} cluster, because of the former's planar, anisotropic structures and larger collision impact parameters.

11.3.1.2.2. Comparison of E_0^{CID} and E_0 , the True Dissociation Threshold. An important finding from the fits of σ_{CID} versus E_{rel} is that the derived values of E_0^{CID} are larger than the actual E_0 thresholds. For Al_6 (O_h) E_0^{CID} is 52.7 kcal/mol, in contrast to $E_0 = 38.8$ kcal/mol. For Al_6 (C_{2h}) $E_0^{CID} = 54.9$ kcal/mol, while E_0 is 43.8 kcal/mol. As a check of the trajectory fit for Al_6 (O_h), an additional calculation was performed at $E_{rel} = 50$ kcal/mol and, of the 600 trajectories calculated, not one transferred sufficient energy for CID to occur. The maximum ΔE_{int} was 37.3 kcal/mol, which gives a maximum $\Delta E_{int}/E_{rel}$ energy transfer value of $37.3/50.0 = 0.75$. The accuracy of the fitted threshold for Al_6 (C_{2h}) was tested by calculating an additional 600 trajectories at each E_{rel} of 53.0, 50.0, and 47.0 kcal/mol. The number of CID events found for these energies are 10, 3, and 0, respectively, which gives cross sections of 1.3, 0.4, and 0.0 \AA^2 . Including these low-energy cross sections in the fit by Eq. (11.22), gives $E_0^{CID} = 52.7$ kcal/mol. This E_0^{CID} value is 2.2 kcal/mol smaller than the one obtained without the three low-energy points, but still 9 kcal/mol larger than E_0 , the true threshold!

The implication from the trajectories is that for $Ar + Al_6$ collisions, with E_{rel} near the actual dissociation threshold, there are no collisions that transfer all of E_{rel} to the cluster, and the fitted CID threshold is not the true dissociation threshold. This is an important point since CID experiments are used to determine thresholds (Su and Armentrout 1993). The actual and CID dissociation thresholds for $Ar + Al_6$ may differ because the system is far from the sudden limit (see following Section 5) for small E_{rel} values. As discussed below, changing the mass of the incident atom, the intermolecular potential, and/or the cluster stiffness can increase the efficiency of energy transfer, so that the CID threshold approaches the true threshold. Given the significance of the $Ar + Al_6$ simulation results, additional work on this system, both experimental and computational, seems warranted. The simulations agree with experimental findings for $Ar + Al_6^+$ CID. Product branching ratios and cross sections have been measured (Jarrold et al. 1987) for CID of Al_n^+ clusters ($n = 3-26$) by Ar atoms at a center-of-mass collision energy of 121 kcal/mol. Al^+ is observed to be the main product for clusters with fewer than 15 atoms. The trajectory results agree with this finding. For Al_6^+ , the experimental cross section is 21 \AA^2 , which is similar to the trajectory value of $20-25 \text{ \AA}^2$.

11.3.1.2.3. Factors Influencing Energy Transfer in Al_6 CID. The effect of varying the incident atom's mass on the energy transfer to Al_6 is illustrated in Table 11.1, where average energies transferred and CID cross sections are listed for $E_{rel} = 120.8$ kcal/mol. As the mass of the incident atom is increased, there is more energy transfer to the cluster and the CID cross section becomes larger. At an incident atom mass of 2-3 times the mass of argon, a limit of 0.45 seems to be reached for the average energy transfer efficiency.

Simulations with the Morse* n and Morse/ n potentials show how cluster stiffness affects $Ar + Al_6$ (O_h) energy transfer. The Morse*1 potential gives the same

TABLE 11.1. Dependence of A + Al₆ (O_h) Energy Transfer on Mass of A

m_A	$\langle \Delta E_{\text{int}} \rangle / E_{\text{rel}}^a$	$\sigma_{\text{CID}} (\text{\AA}^2)$	Fraction CID
$3m_{\text{Ar}}$	0.45	24.8 ± 0.3	0.64
$2m_{\text{Ar}}$	0.43	22.7 ± 0.3	0.59
m_{Ar}	0.40	21.7 ± 0.4	0.56
$m_{\text{Ar}}/2$	0.33	18.2 ± 0.4	0.47
$m_{\text{Ar}}/4$	0.25	12.6 ± 0.3	0.33

^aThe standard deviation of the mean for each value is less than 0.005. Three thousand trajectories were evaluated for each mass of A.

structure and dissociation energy for Al₆ (O_h) as does the L-J/A-T potential, but has slightly different vibrational frequencies. The Morse**n* and Morse/*n* potentials are the same as Morse*1, except their vibrational frequencies are *n* times larger and smaller, respectively.

Calculations for the Al₆ (O_h) Morse potentials were performed with $E_{\text{rel}} = 120.8$ kcal/mol, and the results are given in Table 11.2. The energy transfer efficiency is strongly dependent on cluster stiffness (i.e., efficient for soft clusters and inefficient for stiff clusters), and there appear to be soft and stiff asymptotic limits. For the Morse*1 and softer clusters, energy transfer is efficient and the CID cross section is large (i.e., $>20 \text{\AA}^2$). The average energy transfer to vibration and rotation (i.e., $\langle \Delta E_{\text{vib}} \rangle$ and $\langle \Delta E_{\text{rot}} \rangle$) are also included in Table 11.2. For the soft clusters the transfer is primarily to vibration, but to rotation for the stiff clusters. Transfers to vibration and rotation were not determined for the Morse/4, Morse/2, and L-J/A-T potentials. However, the result for the L-J/A-T potential should be similar to that for the Morse*1 potential. Rotational energy transfer for the Morse/4 and Morse/2 potentials is expected to be lower than for the Morse*1 potential.

TABLE 11.2. Dependence of Ar + Al₆ (O_h) Energy Transfer on the Cluster Stiffness^a

Potential Surface	$\langle \Delta E_{\text{int}} \rangle / E_{\text{rel}}^c$	$\langle \Delta E_{\text{vib}} \rangle$	$\langle \Delta E_{\text{rot}} \rangle$	$\sigma_{\text{CID}} (\text{\AA}^2)$	Fraction CID
Morse/4 ^b	0.48	— ^d	—	26.3 ± 0.3	0.68
Morse/2	0.47	—	—	25.5 ± 0.3	0.66
L-J/A-T	0.40	—	—	21.7 ± 0.4	0.56
Morse*1	0.42	35.5	4.8	23.1 ± 0.3	0.60
Morse*2	0.25	19.4	10.9	13.5 ± 0.3	0.35
Morse*4	0.17	6.3	13.6	6.9 ± 0.3	0.18
Morse*6	0.13	1.5	14.7	4.2 ± 0.2	0.11
Morse*8	0.13	0.6	15.1	3.0 ± 0.2	0.08

^aEnergies are in kcal/mol. The collision energy $E_{\text{rel}} = 120.8$ kcal/mol.

^bThe Morse/*n* potentials have vibrational frequencies *n* times smaller than the actual values, while for the Morse**n* potentials the frequencies are *n* times larger.

^cThe standard deviation of the mean for each value is less than 0.005. Three thousand trajectories were evaluated for each potential surface.

^d $\langle \Delta E_{\text{vib}} \rangle$ and $\langle \Delta E_{\text{rot}} \rangle$ values were not evaluated.

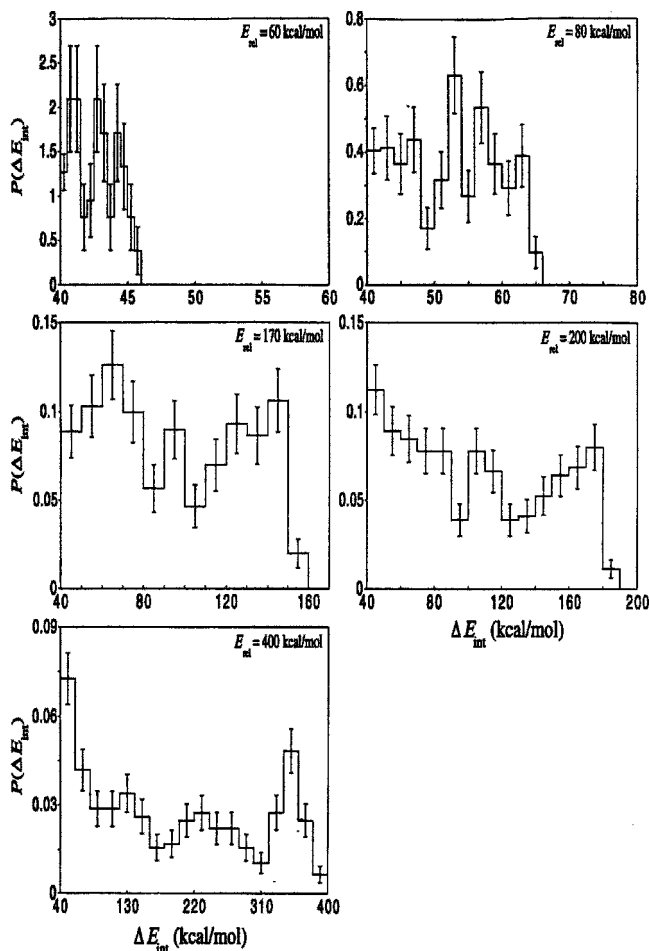


FIGURE 11.4. Energy transfer distributions for $\text{Ar} + \text{Al}_6(\text{O}_h)$ on the L-J/A-T surface for different collision energies. [Reprinted with permission from de Sainte Claire et al. (1995).]

The energy transfer efficiency also depends on the collision energy. Figure 11.3 shows that, for the $\text{Al}_6(\text{O}_h)$ cluster and $E_{\text{rel}} = 120.8$ kcal/mol, the maximum value of ΔE_{int} transferred divided by E_{rel} is ≈ 0.9 . Figure 11.4 shows that, for $\text{Ar} + \text{Al}_6(\text{O}_h)$ collisions, there is a higher probability of transferring large fractions of E_{rel} as E_{rel} is increased. For $E_{\text{rel}} = 400$ kcal/mol, there are collisions in which all of E_{rel} is transferred to ΔE_{int} and the maximum $\Delta E_{\text{int}}/E_{\text{rel}}$ equals unity. For E_{rel} of 60 and 80 kcal/mol, the maximum $\Delta E_{\text{int}}/E_{\text{rel}}$ are much lower: approximately 0.77 and 0.82, respectively. As discussed above, for $E_{\text{rel}} = 50$ kcal/mol the maximum $\Delta E_{\text{int}}/E_{\text{rel}}$ is 0.75. The inability to transfer all of E_{rel} to ΔE_{int} as E_{rel} is decreased, is the origin of E_0^{CID} values from the simulations larger than the true thresholds.

The intermolecular potential between the rare-gas atom and the aluminum cluster also affects the energy transfer. This is illustrated in Figure 11.5, where the CID

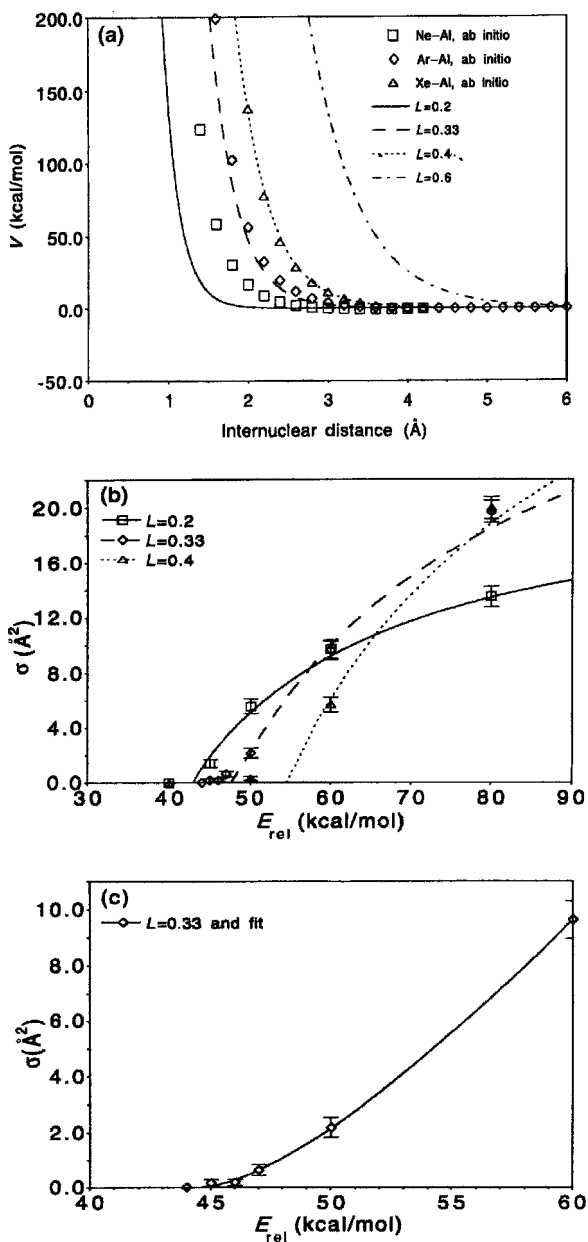


FIGURE 11.5. (a) Different Rg-Al intermolecular potentials. The curves for different L values are plots of Eq. (11.21), with $V_0 = 20,257.938$ kcal/mol. (b) Calculated and fitted σ_{CID} versus E_{rel} for Xe + Al₆, using three of the intermolecular potentials in (a). (c) Fit to the σ_{CID} at low E_{rel} , for the curve in (b) with $L = 0.33$. [Adapted with permission from de Sainte Claire and Hase (1996).]

TABLE 11.3. Fits of Eq. (11.22) to Al₆ (*O_h*) CID Cross Sections versus E_{rel} ^a

Rare Gas	Cluster	Potential		<i>A</i>	E_0^{CID}	<i>n</i>
		Cluster	Intermolecular			
Ar	Al ₆	L-J/A-T	Eq. (11.20)	40.0	52.7	0.99
Xe	Al ₆	L-J/A-T	Eq. (11.21), $L = 0.2^b$	48.3	43.4	0.86
Xe	Al ₆	L-J/A-T	Eq. (11.21), $L = 0.33^b$	63.3(6.91) ^c	48.5(44.9)	0.91(1.61)
Xe	Al ₆	L-J/A-T	Eq. (11.21), $L = 0.4^b$	81.0	55.0	0.90

^a*A* is in units of \AA^2 and E_0^{CID} in kcal/mol. The fits are shown in Figure 11.5.

^b $V_0 = 20,257.938$ kcal/mol and L is in units of \AA .

^cThe numbers in the parentheses are fit to the cross sections at low E_{rel} .

cross sections versus E_{rel} are plotted for Xe + Al₆ (*O_h*), using the L-J/A-T potential for the cluster. The Xe–Al₆ intermolecular potential is written as a sum of Xe–Al two body interactions given by Eq. (11.21), with $V_0 = 20257.938$ and a value of either 0.2, 0.33, or 0.4 for the range parameter L . Both the high-energy, asymptotic value of σ_{CID} and CID threshold increase as L is increased. The former is expected, since the Xe + Al₆ collision radius increases as L is increased. Apparently, increasing L decreases the probability of energy transfer, and as a result the CID threshold increases. Values of the parameters in Eq. (11.22), which give fits to the $\sigma_{\text{CID}}-E_{\text{rel}}$ curves in Figure 11.5, are listed in Table 11.3. The A parameter increases from 48.3 to 81.0 \AA^2 and E_0^{CID} increases from 43.4 to 55.0 kcal/mol, as L is increased from 0.2 to 0.4 \AA . The fitted values of n are near unity, which indicates that a hard-sphere and line-of-centers energy transfer model is appropriate.

For the Xe + Al₆ calculation with $L = 0.33$, σ_{CID} was calculated for a range of low E_{rel} values. Fitting the low E_{rel} points by Eq. (11.22), as shown in the bottom graph in Figure 11.5, gives an E_0^{CID} value only 3–4 kcal/mol lower than that found from the complete $\sigma_{\text{CID}}-E_{\text{rel}}$ curve, which suggests that a meaningful E_0^{CID} value may be obtained by fitting the complete σ_{CID} curve. On the other hand, a value of n significantly larger than unity is obtained for the fits to σ_{CID} at low E_{rel} . This is because near threshold the collisions are not impulsive (Mahan 1970; Yardley 1980; Shin 1976) and the line-of centers models [i.e., Eq. (11.22) with $n = 1$] no longer applies. Values of n larger than unity have been observed in fits of experimental σ_{CID} curves by Eq. (11.22) (Lian et al. 1992; Su and Armentrout 1993).

11.3.1.3. Qualitative Model for Energy Transfer in CID. Insight into the dynamics of energy transfer in CID can be acquired by considering the refined impulsive model developed by (Mahan 1970; Yardley 1980) for translation to vibration ($T \rightarrow V$) energy transfer in collinear A + BC collisions. The model accounts for the mass terms and interactions between the BC vibration and Fourier components of the intermolecular interaction between A and B. For this model, the fraction of initial relative translational energy transferred to BC vibration is

$$\frac{\Delta E}{E_{\text{rel}}} = 4 \cos^2 \beta \sin^2 \beta \left(\frac{\xi}{2} \operatorname{cosech} \frac{\xi}{2} \right)^2 \quad (11.23)$$

where

$$\cos^2 \beta = \frac{m_A m_C}{(m_A + m_B)(m_B + m_C)} \quad (11.24)$$

The ξ term in Eq. (11.23) is often called the *adiabaticity parameter* and is given by

$$\xi = 4\pi^2 \nu L / v_{\text{rel}} \quad (11.25)$$

where ν is the BC vibrational frequency, v_{rel} is the A + BC initial relative velocity, and L is the range parameter for the A–B interaction, given by Eq. (11.21). In this equation r is the A–B internuclear separation. For small ξ the collisions are in the sudden limit, and $\Delta E/E_{\text{rel}}$ reaches its maximum value

$$\frac{\Delta E_{\text{sudden}}}{E_{\text{rel}}} = 4 \cos^2 \beta \sin^2 \beta \quad (11.26)$$

Thus, according to the definition of ξ in Eq. (11.25), energy transfer reaches its maximum efficiency for a small BC vibrational frequency, short-range parameter, and/or large relative velocity between the collision partners. As discussed above, and reviewed below, these are the dynamical properties that give efficient energy transfer in the trajectory simulations of Al_n CID:

Effect of Al_n Vibrational Frequency. Table 11.2 shows that the CID cross section increases as the cluster frequencies are lowered, which is in accord with the impulsive model.

Effect of Rg-Al_n Intermolecular Potential. Table 11.3 and Figure 11.5 show that the efficiency of energy transfer to the Al_n cluster is increased at low E_{rel} as the range parameter L becomes smaller and the Rg-Al interaction becomes more short-range. This is the effect predicted by the adiabaticity parameter.

Effect of Collision Energy. The adiabaticity parameter becomes smaller, and the collision approaches the sudden limit, as the collision velocity v_{rel} is increased. Thus, more efficient energy transfer is predicted at large collision energies. Figure 11.4 illustrates this effect, where at $E_{\text{rel}} = 400$ kcal/mol there are collisions that transfer all of E_{rel} to Al_6 internal energy, while at $E_{\text{rel}} = 60$ kcal/mol the maximum fraction of E_{rel} transferred is 0.77.

Overall, Mahan's impulsive model provides a good qualitative understanding of the energy transfer dynamics for $\text{Rg} + \text{Al}_n$ CID.

11.3.2. Ar Atom Collisions with N-Protonated Glycine and Alanine Polypeptides

Chemical dynamics simulations of N-protonated polyglycine and polyalanine CID (Meroueh and Hase 1999, 2000) are discussed below.

11.3.2.1. Potential Energy Functions. The protonated peptide potential was represented by both the Amber valence forcefield (Cornell et al. 1995) and the AM1 semiempirical electronic structure theory (Dewar et al. 1985; Stewart 1989). For the Amber model the potential is

$$V_{\text{peptide}} = \sum_{\text{bonds}} K_r(r - r_{\text{eq}})^2 + \sum_{\text{angles}} K_{\theta}(\theta - \theta_{\text{eq}})^2 + \sum_{\text{dihedrals}} \frac{V_n}{2}[1 - \cos(n\phi - \gamma)] + \sum_{i>j} [A_{ij}/r_{ij}^{12} - B_{ij}/r_{ij}^6 + q_i q_j / (\epsilon r_{ij})] \quad (11.27)$$

Values for the potential parameters are derived to fit properties of biological molecules (Cornell et al. 1995). For the AM1 model, there is no analytic potential energy function, and instead V_{peptide} and the derivatives of this potential with respect to the Cartesian coordinates are determined at each integration step of the classical trajectory by solving the time-independent Schrödinger equation for the AM1 semiempirical model. Such a calculation is called a direct dynamics simulation (Sun and Hase 2003; Hase et al. 2003). The simulations reported below indicate that either the Amber or AM1 potential energy model may be used to study the dynamics of collisional energy transfer. However, only AM1 may be used to study peptide ion dissociation.

The Ar-peptide intermolecular potential is written as a sum of two-body interactions of the form

$$V(r) = ae^{-br} + \frac{c}{r^9} \quad (11.28)$$

between the Ar atom and the atoms of the peptide. Since high-energy collisions are considered in the CID simulation and the short repulsive region of the intermolecular potential is critical to the energy transfer, no attempt was made to represent the shallow attractive potential energy minima between Ar and the peptide's atoms. The two-body parameters in Eq. (11.28) for the Ar-peptide potential were determined by using the small molecules CH_4 , NH_3 , NH_4^+ , and H_2CO to represent the functional groups for the N-protonated polyglycine and polyaniline peptides. Ab initio calculations, at the QCISD(T)/6-311++G** level of theory, were used to calculate an intermolecular potential between Ar and each of these model molecules. These ab initio potentials were then fit by a sum of the two-body function in Eq. (11.28) to derive parameters for Ar interacting with the atoms of the model molecules; for example, a , b , and c parameters for Ar-H and Ar-C two-body interactions were determined from the Ar- CH_4 ab initio intermolecular potential.

11.3.2.2. Simulation Results. Quasiclassical normal mode sampling was used to select initial coordinates and momenta for the peptide ions. Energies for the peptides normal modes of vibration were selected from their 300 K Boltzmann distribution. A 300 K rotational energy of $RT/2$ was added to each of the peptide's principal axis of

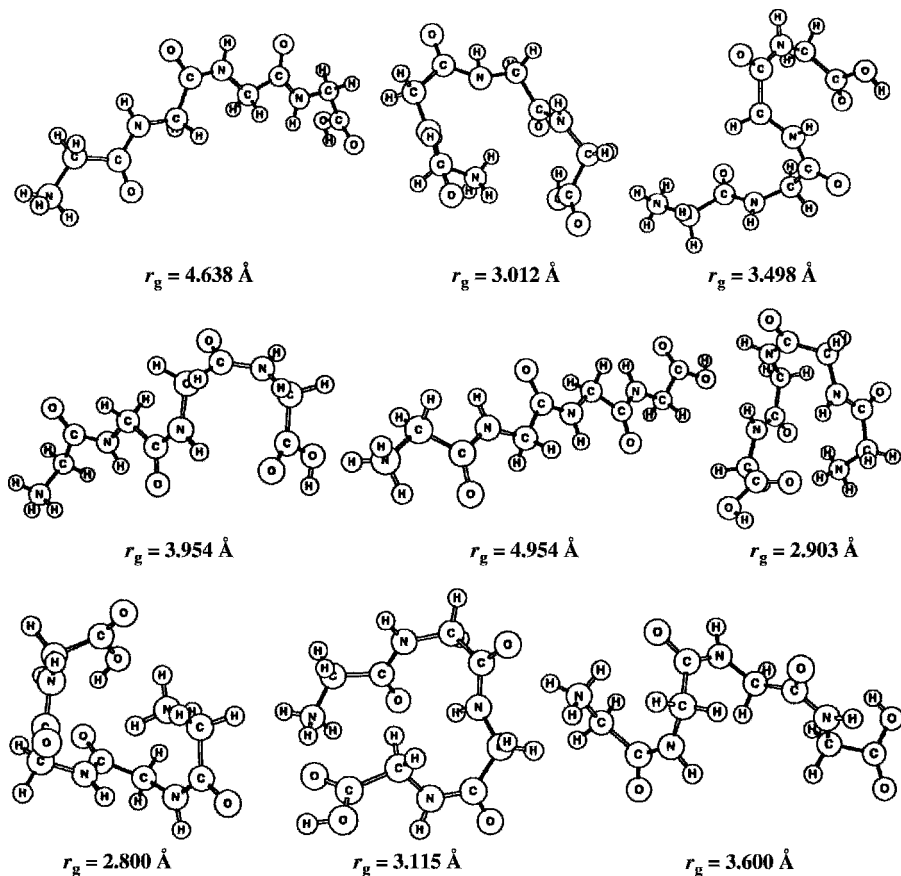


FIGURE 11.6. Structures of $\text{gly}_4\text{-H}^+$ investigated for energy transfer efficiency. The radius of gyration is given for each structure. [Reprinted with permission from Meroueh and Hase (1999).]

rotation. Argon–peptide collision energies of 100, 500, and 1000 kcal/mol were considered with the energy transfer dynamics studied versus impact parameter b . Different polypeptide structures were investigated and those for protonated tetraglycine ($\text{gly}_4\text{-H}^+$) are shown in Figure 11.6. The results of the simulations are described in the following text.

11.3.2.2.1. Comparison of Amber and AM1 Peptide Intramolecular Potentials. Amber represents the vibrational motion of the peptide ions and, thus, may be used to model collisional energy transfer to the peptide. However, since Amber is a molecular mechanics (MM) model, it does not describe the peptide ion's dissociation pathways. An important question is whether this incompleteness in the Amber potential affects the collisional energy transfer in the simulations. This question was addressed by also using the AM1 semiempirical quantum chemistry

model for the peptide ion's potential in direct dynamics simulations of Ar + peptide-H⁺ and peptide-H⁺ + surface collisional energy transfer (Meroueh et al. 2002; Wang et al. 2003b). The peptide ions considered are gly-H⁺ and gly₂-H⁺. What was discovered is that the Amber and AM1 models for the peptide-H⁺ intramolecular potential give the same efficiencies for collisional energy transfer. The comparison for Ar + gly-H⁺ at $E_i = 70$ eV, $\theta_i = 45^\circ$, and $b = 0$ is shown in Figure 11.7. For the Amber potential the percent energy transfers to ΔE_{int} , ΔE_{surf} , and E_f are 11, 37, and 52, respectively. Using AM1 potential, these percentages are nearly identical: 12, 38, and 50. A similar result is found for collisional energy transfer to the gly₂-H⁺ peptide. Thus, these calculations show that the Amber potential may be used to study collisional energy transfer in peptide-H⁺ CID, and the results described below were determined using AMBER for the peptide-H⁺ intramolecular potential. The agreement between the AMBER and AM1 energy transfer efficiencies for both gly-H⁺ and gly₂-H⁺, indicates the agreement is not coincidental and both models adequately represent the peptide-H⁺ intramolecular potential. Thus Amber, which is more computationally efficient, may be used to study the dynamics of energy transfer.

11.3.2.2.2. Role of the Collision Impact Parameter. The percent energy transfer to the internal degrees of freedom of β -sheet polyglycine peptides [i.e., β -(gly_{*n*}-H⁺)] are shown in Figure 11.8 as a function of the collision impact parameter b for $n = 2-7$ and a collision energy of 100 kcal/mol. As one would expect, the average fraction of energy transfer decreases with increase in impact parameter, with the most rapid decline for the smallest peptide. At $b = 0$ the peptides have average energy transfer efficiencies in the range $\sim 50-60\%$. The largest b at which measurable energy transfer occurs varies from 7 to 16 Å in going from β -(gly₂-H⁺) to β -(gly₇-H⁺).

Because of a finite energy transfer for all impact parameters, unambiguously defining b_{max} remains a difficult problem if one wishes to determine the complete energy transfer distribution curve $P(\Delta E_{\text{int}})$, starting with $\Delta E_{\text{int}} = 0$. In contrast, if the $P(\Delta E_{\text{int}})$ that is of interest is the one with $\Delta E_{\text{int}} > E_0$, where E_0 is the ion's dissociation threshold, an unambiguous b_{max} may be determined. A quantity that may be converged from the trajectory simulations is the average energy transfer versus impact parameter $\langle \Delta E(b) \rangle$ integrated over the differential cross section $2\pi b db$ (Peslherbe et al. 1999):

$$\langle \Delta E \rangle_\sigma = \int_0^\infty \langle \Delta E(b) \rangle 2\pi b db \quad (11.29)$$

Values for $\langle \Delta E \rangle_\sigma$ versus the size of the β -(gly_{*n*}-H⁺) peptide increase nearly linearly from 1000 kcal Å²/mol for β -(gly₂-H⁺) to 7169 kcal Å²/mol for β -(gly₇-H⁺), for $E_{\text{rel}} = 100$ kcal/mol. A value for $\langle \Delta E \rangle$, the average energy transfer averaged over b , may be determined by dividing $\langle \Delta E \rangle_\sigma$ by an assumed collision cross section πb_{max}^2 . The collision cross section is often equated to the Lennard-Jones cross section (Whyte et al. 1988).

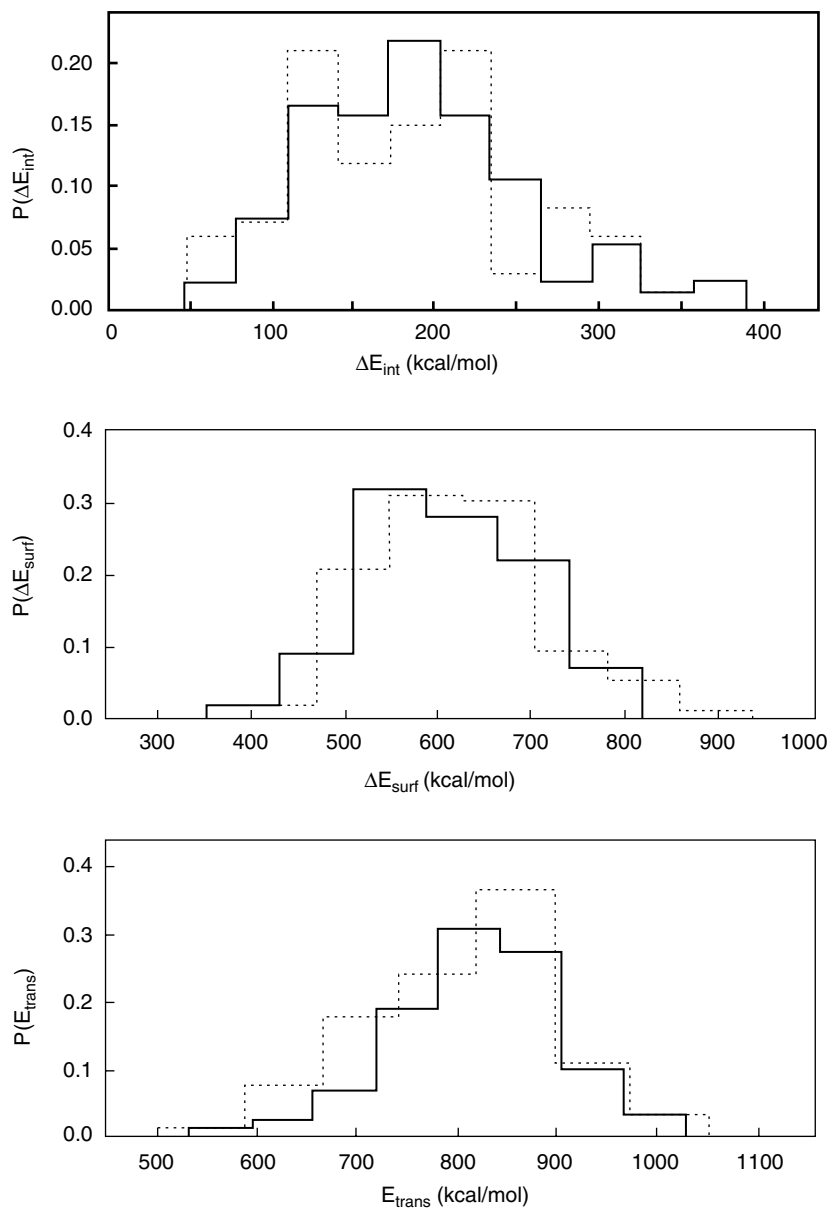


FIGURE 11.7. Distributions of the energy transfer to (gly- H^+) vibration/rotation ($E_i \rightarrow E_{\text{int}}$), the surface ($E_i \rightarrow E_{\text{surf}}$), and translation ($E_i \rightarrow E_{\text{trans}}$) for the (gly- H^+) intramolecular potential represented by the AMBER force field (—) and AM1 (···). Results for (gly- H^+) colliding with diamond {111} at an initial energy and angle of 70 eV and 45° . [Reprinted with permission from Meroueh et al. (2002).]

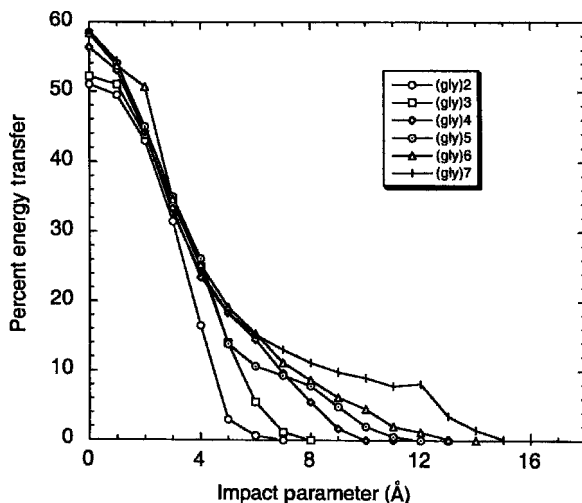


FIGURE 11.8. Percent energy transfer to β -(gly₄-H⁺) structures versus impact parameter at $E_{\text{rel}} = 100$ kcal/mol. [Reprinted with permission from Meroueh and Hase (1999).]

11.3.2.2.3. Peptide Size and Collision Energy. The effect of peptide size and collision energy on collision activation was studied by determining the average energy transfer for the collision of Ar with both polyglycines and polyalanines at E_{rel} of 100, 500, and 1000 kcal/mol. Extended β -sheet structures were considered for the polyglycines, while these structures as well as folded, α -helix structures were considered for the polyalanines. The structures are given in Meroueh and Hase (1999). To circumvent the need to choose a value for b_{max} , the simulations were performed for $b = 0$.

The percent energy transfers are shown in Figure 11.9. As is discussed in Section 11.3.1.3, in the impulsive sudden limit the percent energy transfer would be independent of the peptide and E_{rel} . Overall the percent energy transfer values are inconsistent with this model. At $E_{\text{rel}} = 100$ kcal/mol there is a linear-like increase in the percent energy transfer versus the number of atoms for each of the polypeptides. The compounds β -(gly_{*n*}-H⁺) and α -(ala_{*n*}-H⁺), with the same number of atoms, have similar energy transfer efficiencies. The energy transfers are somewhat smaller for β -(ala_{*n*}-H⁺). Different energy transfer patterns are observed at E_{rel} of 500 and 1000 kcal/mol as compared to $E_{\text{rel}} = 100$ kcal/mol. At these higher E_{rel} , the percent energy transfer to the different size β -sheet peptides shows no apparent trend, with a variation of only 4%. On the other hand, for α -(ala_{*n*}-H⁺) the percent energy transfer retains a near-linear increase. Another identifier in the difference between the energy transfer dynamics, at E_{rel} of 100 kcal/mol as compared to 500 and 1000 kcal/mol, is the similar range of percent energy transfer values at 500 and 1000 kcal/mol, which are significantly larger than those at 100 kcal/mol. The picture from these simulations is that energy transfer to the β -sheet peptides attains the sudden limit between E_{rel} of 100 and 500 kcal/mol, while an E_{rel} larger than 1000 kcal/mol

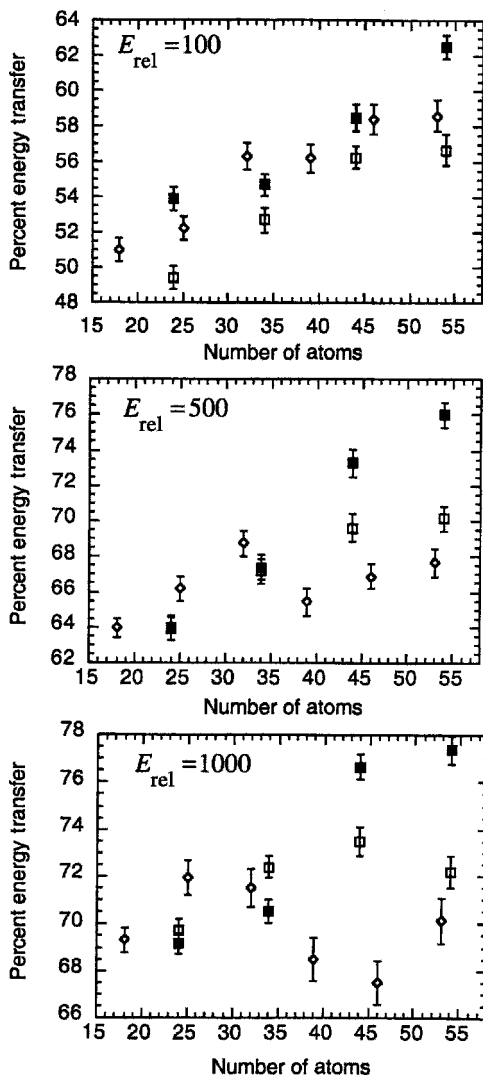


FIGURE 11.9. Percent energy transfer at $b = 0$ versus size of gly_n-H⁺ and ala_n-H⁺ polypeptides for E_{rel} of 100, 500, and 1000 kcal/mol: (■) β -(gly_n-H⁺) and (□) α -(ala_n-H⁺); (◇) β -(gly_n-H⁺). [Reprinted with permission from Meroueh and Hase (1999).]

is required to reach the sudden limit for α -(ala_n-H⁺). At $E_{\text{rel}} = 3000$ kcal/mol α -(ala₂-H⁺) and α -(ala₅-H⁺) have statistically the same energy transfer efficiencies of 67% and 69%, respectively.

11.3.2.2.4. Peptide Structure. The role of the peptide structure in the collision activation was investigated in detail by considering a range of structures for gly₄-H⁺, shown in Figure 11.6. Each structure is characterized by its radius of gyration r_g ,

defined as

$$r_g = \left(\frac{\sum r_i^2}{n+1} \right)^{1/2} \quad (11.30)$$

where the r_i are the distances of the n atoms from the peptide's center of mass. Collisions of Ar with these $\text{gly}_4\text{-H}^+$ structures were studied for $b = 0$ and $E_{\text{rel}} = 100$ kcal/mol and 1000 kcal/mol.

The simulation results are given in Figure 11.10 and it is seen that, even though the collisions are head-on with $b = 0$, the structure of the peptide affects the efficiency of energy transfer. For the $E_{\text{rel}} = 100$ kcal/mol collision, there is a near-linear 15% decrease in the percent energy transfer as r_g increases from 3 to 5 Å. At $E_{\text{rel}} = 1000$ kcal/mol this linear trend is not observed. However, there is still a predominant decrease in the energy transfer efficiency as r_g is increased. The general result from these calculations is that the more compact, folded structures give more efficient energy transfer.

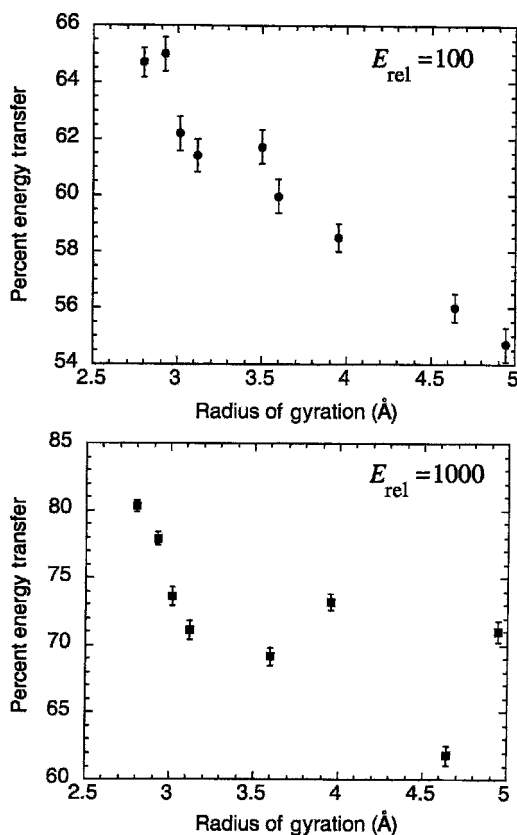


FIGURE 11.10. Percent energy transfer at $b = 0$ and E_{rel} of 100 and 1000 kcal/mol for $\text{gly}_4\text{-H}^+$ structures in Figure 11.6. [Reprinted with permission from Meroueh and Hase (1999).]

The trends in the energy transfer efficiencies versus r_g for E_{rel} of 100 and 1000 kcal/mol are consistent with the discussion in the previous section concerning the sudden limit for energy transfer. At $E_{\text{rel}} = 100$ kcal/mol, the energy transfer is not in the sudden limit and it depends on the peptide structure. At the larger E_{rel} of 1000 kcal/mol some of the peptides are in the sudden limit and have similar energy transfers.

Although the $b = 0$ energy transfer efficiencies depend on peptide structure, the quantity $\langle \Delta E \rangle_\sigma$ in Eq. (11.29) appears to be relatively independent of peptide structure (Meroueh and Hase 2000). $\langle \Delta E \rangle_\sigma$ increases near linearly with increase in E_{rel} for β -(gly₄-H⁺) and α -(gly₄-H⁺), suggesting b_{max} and percent energy transfer values that are only weakly dependent on E_{rel} (see Figure 11.9). At $E_{\text{rel}} = 100$ kcal/mol, these two peptides structures have nearly identical $\langle \Delta E \rangle_\sigma$ values, while for $E_{\text{rel}} = 1000$ kcal/mol $\langle \Delta E \rangle_\sigma$ is 20% larger for β -(gly₄-H⁺).

11.3.2.2.5. $T \rightarrow V$ versus $T \rightarrow R$ Energy Transfer. In Section 11.3.1.2.1, it is shown that the energy transfer is primarily translation to vibration ($T \rightarrow V$) for the spherically shaped Al_n clusters, with $\sim 40\%$ of the transfer is translation to rotation ($T \rightarrow R$) for planar Al_n clusters. A similar effect is found for the polypeptides. A comparison of $T \rightarrow V$ and $T \rightarrow R$ energy transfers, for β -(gly₄-H⁺) and α -(gly₄-H⁺), is shown in Figure 11.11 as a function of b for $E_{\text{rel}} = 100$ kcal/mol. At small impact parameters the energy transfer is primarily to vibration, with transfer to rotation becoming more important as the impact parameter is increased. For the extended β -(gly₄-H⁺) structure, energy transfer to rotation and vibration become similar at the larger impact parameters. For the extended peptide energy transfer becomes negligible at b of ~ 10 Å, whereas for the more compact α -(gly₄-H⁺) peptide it becomes negligible at ~ 7 Å. These are approximate values for b_{max} .

A more quantitative value for b_{max} may be determined from $\langle \Delta E \rangle_\sigma$ in Eq. (11.29), which equals 3638 and 3207 kcal Å²/mol for extended and folded gly₄-H⁺, respectively. Decreasing the upper limit of the integral in Eq. (11.29) will give $\langle \Delta E \rangle_\sigma$ values that are smaller than the limiting value. Tests show that there is a value for the upper limit that, when varied by a very small amount, gives values of $\langle \Delta E \rangle_\sigma$, which are in the range of $1-10^{-4}$ % of the limiting value. This upper limit identifies a value of b_{max} . Setting it so that the value of $\langle \Delta E \rangle_\sigma$ is within 10^{-4} % of the limiting value gives b_{max} of 10.2 and 7.6 for β -(gly₄-H⁺) and α -(gly₄-H⁺), respectively. The average values of the energy transfer are then $\langle \Delta E \rangle_\sigma / \pi b_{\text{max}}^2$ and equal 11.1 and 17.5 kcal/mol for the extended and folded gly₄-H⁺ peptides, respectively. Writing $\langle \Delta E(b) \rangle$ in Eq. (11.29) as the sum $\langle \Delta E_{\text{vib}}(b) \rangle + \langle \Delta E_{\text{rot}}(b) \rangle$ and taking $\langle \Delta E_{\text{vib}}(b) \rangle$ and $\langle \Delta E_{\text{rot}}(b) \rangle$ from Figure 11.11, the average transfers to vibration and rotation, averaged over b , are found to be $\langle \Delta E_{\text{vib}}(b) \rangle = 7.7$ kcal/mol and $\langle \Delta E_{\text{rot}}(b) \rangle = 3.4$ kcal/mol for the extended β -(gly₄-H⁺) peptide and $\langle \Delta E_{\text{vib}}(b) \rangle = 14.5$ kcal/mol and $\langle \Delta E_{\text{rot}}(b) \rangle = 3.0$ kcal/mol for the folded α -(gly₄-H⁺) peptide. Thus 31% and 14% of the energy transfer is to rotation for the extended and folded gly₄-H⁺ structures, respectively. These numbers are quite precise given the large number of trajectories calculated. Their accuracy depends on the accuracy of the model for the potential energy function.

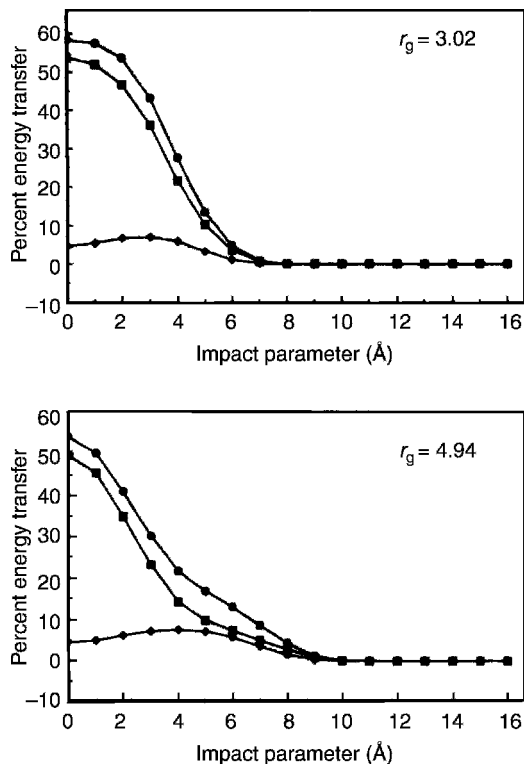


FIGURE 11.11. Total percent energy transfer (circles) and percent energy transfer to vibration (squares) and rotation (diamonds) versus impact parameter for collisions with $E_{\text{rel}} = 100$ kcal/mol and $T_{\text{peptide}} = 300$ K. Results for the folded ($r_g = 3.02$ Å) and extended ($r_g = 4.94$ Å) $\text{gly}_4\text{-H}^+$ peptides. [Reprinted with permission from Meroueh and Hase (2000).]

11.3.2.2.6. Pathways for Energy Transfer. Two important components of the mechanism of energy transfer for the peptide- H^+ are (1) the peptide modes that receive the energy and (2) the nature of the collision between the rare-gas atom and the peptide. The efficiency of energy transfer to specific modes of $\beta\text{-(gly}_4\text{-H}^+)$ was studied by constraining different sets of internal coordinates. This was accomplished by increasing the force constants for a set of internal coordinates so that their vibrations are in the “stiff limit” and do not accept energy. Using H to identify a “heavy” atom such as C, N, or O and L to identify the “light” hydrogen atom, the internal coordinates were grouped into the following sets: HL stretches, HH stretches, LHL bends, HHH bends, HHHL torsions, and HHHH torsions. Calculations were performed for $E_{\text{rel}} = 100$ kcal/mol and $b = 0$, using the $\beta\text{-(gly}_4\text{-H}^+)$ peptide initially in its classical potential energy minimum with no rotational energy. The percent energy transfers with different sets of internal coordinates constrained are listed in Table 11.4.

Constraining the stretches and bends has a small effect on the energy transfer. With no constraints, 58% of the collision energy is transferred to $\beta\text{-(gly}_4\text{-H}^+)$

TABLE 11.4. Percent Energy Transfer to Extended Gly₄-H⁺ with Specific Internal Coordinates Constrained^a

Coordinates Constrained ^b	$E_{\text{rel}} = 100^c$
None	58 (4) ^d
HL stretches	56 (4)
HH stretches	56 (4)
All stretches	57 (4)
LHL bends	57 (5)
HHL bends	56 (5)
HHH bends	55 (5)
All bends	53 (5)
All bends and stretches	49 (6)
HHHL torsions	37 (9)
HHHH torsions	31 (9)
All bends and dihedrals	11 (11)
All	13 (13)

^aThe calculations are for $E_{\text{rel}} = 100$ kcal/mol and $b = 0$. The peptide is initially in its classical potential energy minimum.

^bH corresponds to a heavy atom (i.e., C, N, or O); L corresponds to the light hydrogen atom.

^cEnergy is in kcal/mol.

^dThe standard deviation in the mean percent energy transfer is approximately 1%. The percent energy transfer to rotation is given in parentheses.

internal energy. With all the stretches constrained, this percent is lowered to 57%. With all the bends constrained, the energy transfer is 53%. Constraining both stretches and bends, with only the torsions available for receiving the collision energy, lowers the energy transfer to 49%. This shows that $0.49/0.58 \times 100 = 84$ of the initial energy transfer is to the torsional modes. More energy is transferred to peptide rotation as modes are constrained, and thus there is less energy transfer to vibration. With no constraints the overall energy transfer is 58% with only 4% to rotation. However, with all the modes constrained there is no energy transfer to vibration, but 13% to rotation.

In the simplest model for collision energy transfer (discussed below), there is an impulsive collision between Ar and the peptide with only one inner turning point in their relative motion. Some of the collisions are of this type, but the dominant collisions are indirect events with multiple Ar-peptide encounters. The nature of the collisions may be monitored by calculating the internal energy of the peptide during the collision. Two typical collisions are depicted in Figure 11.12 for Ar + α -(ala₅-H⁺), with an impact parameter of zero and a collision energy of 100 kcal/mol. One of the collisions is direct with only one Ar-peptide encounter. The other is indirect with multiple encounters, identified by the sharp changes in the slope of the peptide's internal energy versus time. The direct collision has an encounter time of ~ 100 fs, while the indirect collision with multiple encounters has a total encounter time of ~ 180 fs. The indirect collision has as many as five encounters.

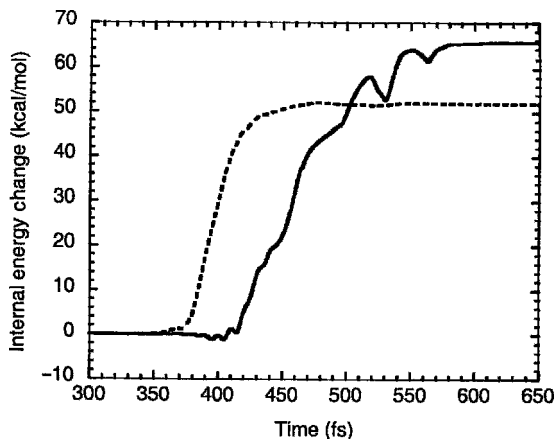


FIGURE 11.12. Examples of a direct trajectory (---) and an indirect trajectory (—) with multiple encounters for $\text{Ar} + \alpha\text{-(ala}_5\text{-H}^+)$ at $E_{\text{rel}} = 100$ kcal/mol and an impact parameter of zero. The internal energy change is that for the peptide. [Reprinted with permission from Meroueh and Hase (1999).]

The relative number of trajectories with a direct encounter, two encounters, and multiple encounters were determined for ten trajectories calculated at different collision energies for three protonated peptides. The results are listed in Table 11.5. Although there are no extraordinary differences in the nature of the encounters for the three peptides, $\beta\text{-(gly)}_7$ appears to have more direct encounters. Such a possible effect needs to be investigated by studying more trajectories. The encounter times range from 40 to 300 fs, with average total encounter times ranging from 80 to 180 fs. More than 50% of the trajectories for each peptide and collision energy have two or more encounters. This effect must be incorporated into any theoretical model describing the efficiency of energy transfer in peptide

TABLE 11.5. Relative Number of Encounters and Average Total Encounter Time for Ar-Protonated Peptide Collisions^a

E_{rel}	Relative Number of Encounters ^b	Range of Encounter Times ^c	Average Total encounter Time ^b
100	1 : 3 : 6	Ar + $\beta\text{-(gly)}_4$ 70–135	100
100	4 : 1 : 5	Ar + $\beta\text{-(gly)}_7$ 55–300	145
100	1 : 2 : 7	Ar + $\alpha\text{-(ala)}_5$ 120–250	180
1000	1 : 6 : 3	40–125	80

^aThe collision impact parameter is zero. Ten trajectories were calculated for the Ar-peptide collisions at each collision energy E_{rel} .

^bRelative number of trajectories with (one encounter): (two encounters): (multiple encounters).

^cThe encounter time is given in fs.

collisional activation. In comparing this rather incomplete analysis for the three peptides and the two different collision energies, the total encounter time tends to increase as the peptide size is increased or E_{rel} is decreased. The results for α -(ala₅-H⁺) and β -(gly₇-H⁺) suggest that the folded peptide may have more multiple encounters and larger total encounter times. Clearly, more work needs to be done to investigate the mechanism for collisional activation of protonated peptide ions. Multiple encounters are expected to enhance the efficiencies of collisional energy transfer.

11.3.2.3. Comparisons with Mahan's Impulsive Energy Transfer Model. Equations (11.23)–(11.26) represent the impulsive model developed by Mahan for $T \rightarrow V$ energy transfer in $A + BC$ collisions. In this model, energy transfer is controlled by the adiabaticity parameter ξ in Eq. (11.25), with the efficiency of energy transfer increasing as ξ becomes smaller. Decreasing the BC vibrational frequency, increasing the collision relative velocity, or decreasing the intramolecular range parameter L , and making the collision less repulsive, decreases ξ and increases energy transfer. As discussed above, this model provides a meaningful interpretation of energy transfer in collisions of Al_n^+ clusters with rare gas atoms and it is of interest to investigate its applicability to Ar^+ peptide-H⁺ collisions.

As the size of a gly_{*n*}-H⁺ or ala_{*n*}-H⁺ peptide increases, the distribution of vibrational frequencies for the peptide extends to lower values and, in an average sense, ξ decreases if E_{rel} held constant. Thus, if the collisions are not in the sudden limit, more efficient energy transfer is expected as n is increased. This is the behavior observed for both the β -sheet and α -helix peptides at E_{rel} of 100 kcal/mol (see Figure 11.9), where there is a near-linear increase in the percent energy transfer as n is increased. In the high-collision-energy sudden limit, when $\xi \ll 1$, the energy transfer should be nearly independent of peptide size, and this is the behavior seen for the β -(ala_{*n*}-H⁺) and β -(gly_{*n*}-H⁺) peptides at $E_{\text{rel}} = 1000$ kcal/mol. However, as discussed above, a higher E_{rel} is required to attain the sudden limit for the α -(ala_{*n*}-H⁺) peptides.

We have seen above that Mahan's model provides at least a qualitative interpretation of the efficiency of energy transfer with respect to peptide size and the collision energy. However, since peptides with the same vibrational frequencies, mass, and intermolecular potential are predicted to have the same energy efficiency according to Mahan's model, this model does not provide a qualitative interpretation of the dependence of the energy transfer efficiency on peptide structure (see Figure 11.10). This is exemplified by the results for the different gly₄-H⁺ structures. The energy transfer efficiency to the peptide varies by up to 15% as its structure is changed. At E_{rel} of 1000 kcal/mol, Figure 11.10 shows that peptides with very different structures may have similar energy transfer efficiencies, which suggests that some of the peptide structures may have reached the sudden limit.

The manner in which a change in the Ar/peptide intermolecular potential affects energy transfer is qualitatively explained by Mahan's model. The simulations presented above were performed with an accurate ab initio Ar^+ peptide-H⁺

intermolecular potential, as described in Section 11.3.2.1. If a molecular-mechanics (MM)-based empirical potential is used, substantially different energy transfer efficiencies are found (Meroueh and Hase 1999). This empirical potential has range parameters L that are ~ 2.5 times smaller than the ab initio values and gives energy transfer efficiencies for $\text{Ar} + \beta\text{-(gly)}_n\text{-H}^+$, where $n = 2-7$, as much as 30% larger than those discussed above for the ab initio potential. As shown by Eqs. (11.23) – (11.26), this increase in energy transfer efficiency with decrease in L agrees with Mahan's model.

Finally, it must be emphasized that Mahan's impulsive model does not provide a means to quantitatively interpret the energy transfer dynamics for collisions with multiple encounters as illustrated in Figure 11.12. Considerable work needs to be done to develop a theoretical model that provides a quantitative understanding of how the peptide size, structure, and amino acid constituents, the collision's intermolecular potential, and the multiple encounters during a collision affect the energy transfer dynamics for peptide- H^+ CID. Simulations such as those discussed here, which address all of these issues, should provide the information needed to develop an accurate theoretical model for energy transfer in peptide- H^+ CID.

11.4. SIMULATIONS OF SID

Trajectory simulations of $\text{Cr}^+(\text{CO})_6$ (Bosio and Hase 1998; Meroueh and Hase 2001; Song et al. 2003) and protonated peptide ion (Meroueh and Hase 2002; Meroueh et al. 2002; Wang et al. 2003a,b) collisions with surfaces have provided fundamental information concerning the energy transfer and fragmentation dynamics of surface-induced dissociation (SID). The results of these simulations are reviewed here. We begin by describing the construction of potential energy surfaces needed for the simulations.

11.4.1. Potential Energy Surfaces for SID Simulations

11.4.1.1. $\text{Cr}^+(\text{CO})_6$. Collisions of $\text{Cr}^+(\text{CO})_6$ with both diamond {111} and alkyl thiolate self-assembled monolayer (H-SAM) surfaces have been simulated. The potential energy function for each of these simulations is represented by Eq. (11.4). The V_{surface} potential for diamond {111} consists of harmonic stretches and bends, with parameters chosen to fit the diamond phonon spectrum (Hass et al. 1992). The surface potential for the SAM is written as

$$V_{\text{SAM}} = V_{\text{inter}} + V_{\text{intra}} \quad (11.31)$$

and is an extension of the potential by Mar and Klein (Mar and Klein, 1994) to represent the 300 K structure of alkyl thiolate SAMs on Au{111}. The SAM's intramolecular potential V_{intra} is a molecular mechanics potential, [Eq. (11.27)] and includes all the stretch, bend, dihedral, and torsional motions of the alkyl thiolate chains. The intermolecular part of the SAM potential is written as the following sum

of two-body terms

$$V_{\text{inter}} = \sum_{\text{C,H}} V_{ij}(r) + \sum_{\text{C,S,H}} V_{i,\text{S}}(r) + \sum_{\text{CH}_2, \text{CH}_3} V_{i,\text{Au}}(z) \quad (11.32)$$

where r is the distance between atom pairs and z is a generalized coordinate representing the distance of a CH_2 or CH_3 group from the Au surface. For the Mar–Klein SAM potential, the Buckingham function

$$V(r) = A \exp(-Br) - C/r^6 \quad (11.33)$$

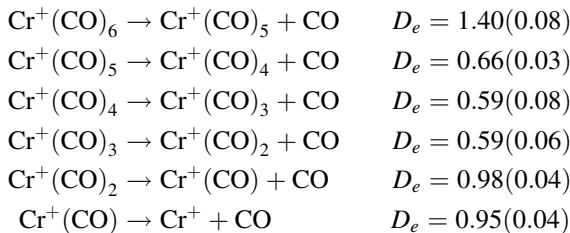
is used for the first two terms in Eq. (11.32). Buckingham-type potentials have the disadvantage of becoming attractive at sufficiently small internuclear separations, which approaches negative infinity as the separation decreases. For the C–H and H–H Buckingham potentials, the barriers for the transition from the repulsive short-range interaction to the unphysical short-range attractive interaction were sufficiently low that they were surmounted by the high-energy SID simulations. To correct this shortcoming, switching functions were used to connect the long-range (LR) C–H and H–H Buckingham potentials to the short-range (SR) Buckingham potentials determined from ab initio calculations (Meroueh and Hase 2001).

The potential energy function for $\text{Cr}^+(\text{CO})_6$ is given by (Meroueh and Hase 2001)

$$\begin{aligned} V = & \sum_{\text{CrC}} D(\Omega) \{1 - \exp[-\beta(r - r_e)]\}^2 \\ & + \sum_{\text{CrC}} \Delta D(\Omega) + \sum_{\text{CO}} k_R (R - R_e)^2 \\ & + \sum_{\text{CrCO}} \frac{k_\phi}{2} (\phi - \phi_e)^2 + \sum_{\text{CCrC}} \frac{k_\theta}{2} (\theta - \theta_e)^2 \end{aligned} \quad (11.34)$$

where a Morse function is used for the Cr–C stretches and harmonic terms are used for the other degrees of freedom. The force constant for each ϕ and θ bending potential is attenuated, so that the force constant goes to zero as a Cr–C bond defining the bend angle ruptures.

The $D(\Omega)$ and $\Delta D(\Omega)$ terms in Eq. (11.34) are determined as follows. Experiments have shown that the Cr–CO bond dissociation energy depends on the extent of dissociation (Khan et al. 1993) and varies according to



where D_e is in units of eV and the values in the parentheses are the uncertainties. To represent these changes in the Cr–C dissociation energy, D_e is written as a function of the extent of dissociation defined by

$$\Omega = \sum_{i=1}^6 \frac{1}{r_i} \quad (11.35)$$

The value of Ω for a $\text{Cr}^+(\text{CO})_n$ complex is evaluated by setting r_i for the ruptured bonds to ∞ and r_i for the intact bonds to their equilibrium value. The Cr–C bond dissociation is written as a function of Ω to fit the values listed above and give $D(\Omega)$. As additional Cr–C bonds rupture, the dissociation energy of the ruptured bonds must be shifted to maintain the proper total potential energy for the ruptured bonds. This is accomplished by $\Delta D(\Omega)$.

Two-body intermolecular potentials, for the Cr^+ , C, and O atoms of $\text{Cr}^+(\text{CO})_6$ interacting with the H and C atoms of the diamond {111} and H-SAM surfaces, were determined from ab initio calculations (Meroueh and Hase 2001) as described in Section 11.3.2.1 for the Ar + peptide– H^+ potentials. The ab initio calculations were performed for Cr^+ and CO interacting with CH_4 as a representative of the H and C atoms on the surface. The Cr^+ –H and Cr^+ –C potentials are given by

$$V(r) = A \exp(-Br) + C/r^6 + D/r^4 \quad (11.36)$$

The D/r^4 term is included to model the charge-induced dipole interaction. The same potential function is used for the interactions of the C and O atoms of $\text{Cr}^+(\text{CO})_6$ with the C and H atoms of the surfaces, except the D/r^4 term is not included. Also, C/r^6 is replaced by the more general term C/r^d . The ab initio calculations for the Cr^+/CH_4 system were carried out at the UMP2/6-311+G(3df) level of theory. While those for CO/CH_4 used the MP2/aug-cc-pVTZ level of theory.

11.4.1.2. Peptide– H^+ . For the peptide– H^+ SID simulations, the potentials used for diamond {111} and the H-SAM are the same as those described above for $\text{Cr}^+(\text{CO})_6$. Both the empirical Amber and the AM1 semiempirical electronic structure theory models were used for the peptide ion's intramolecular potential (see Section 11.3.2.1): $V_{\text{projectile}}$ in Eq. (11.4). An intermolecular potential, for the peptide ion interacting with the surface, was developed in the same manner as described in Section 11.3.2.1 for the Ar/peptide– H^+ intermolecular potential. The peptide/surface intermolecular potential is modeled by a sum of two-body potentials between the atoms of the peptide and surface. The two-body potentials are given by the Buckingham function in Eq. (11.33).

To determine the parameters for the two-body potentials, ab initio potential energy curves were calculated between CH_4 , as a model for the C and H atoms of diamond {111} and *n*-hexyl thiolate SAM surfaces, and CH_4 , NH_3 , NH_4^+ , H_2CO , and H_2O , as models for the different types of atoms and functional groups representing the protonated polyglycine and polyalanine peptides. The ab initio calculations are carried out at the MP2 level theory with the 6-311+G(2df,2pd) basis set. The molecules were held fixed in their optimized geometries and intermolecular

potential energy curves for different orientations of CH_4/CH_4 , CH_4/NH_3 , $\text{CH}_4/\text{NH}_4^+$, $\text{CH}_4/\text{H}_2\text{CO}$, and $\text{CH}_4/\text{H}_2\text{O}$ systems were calculated. These curves were then fit to determine the two-body potential parameters.

11.4.2. SID Simulation Results

The results obtained from simulations of $\text{Cr}^+(\text{CO})_6$ and peptide- H^+ SID on H-SAM and diamond {111} surfaces are summarized in Table 11.6. The simulations provide

TABLE 11.6. Dynamics of SID from Trajectory Simulations

Projectile(s)	Chemical Dynamics Result	Ref.
$\text{Cr}^+(\text{CO})_6$	Shattering dissociation with H-SAM and diamond surfaces; shattering on the H-SAM requires a higher E_i	Meroueh and Hase (2001), Song et al. (2003)
$\text{Cr}^+(\text{CO})_6$	Negligible energy transfer to CO vibration during collision with or after rebounding off surface	Song et al. (2003)
$\text{Gly}_3\text{-H}^+$, $\text{Cr}^+(\text{CO})_6$	Very different energy transfer distributions for collisions with H-SAM and diamond surfaces; for $\text{gly}_3\text{-H}^+$ collisions at $E_i = 30$ eV, the average percent transfers to ΔE_{int} , ΔE_{surf} , and E_f are 20, 8, and 72 for diamond and 8, 54, and 38 for H-SAM. ^a	Meroueh and Hase (2001, 2002); Song et al. (2003)
$\text{Gly}_n\text{-H}^+$	Energy transfer is very similar for $\text{gly}_3\text{-H}^+$ and $\text{gly}_5\text{-H}^+$	Meroueh and Hase (2002)
$\text{Gly}_3\text{-H}^+$	Folded and extended structures for $\text{gly}_3\text{-H}^+$ give similar energy transfer efficiencies	Meroueh and Hase (2002)
$\text{Gly}_n\text{-H}^+$, $\text{Cr}^+(\text{CO})_6$	Percent energy transfer to ΔE_{int} is only weakly dependent on E_i , while percent transfer to ΔE_{surf} and E_f increases and decreases, respectively, with increase in E_i	Meroueh and Hase (2002); Song et al. (2003); Wang et al. (2003a).
$\text{Gly}_3\text{-H}^+$	In collisions with diamond at 30 eV, 80% of ΔE_{int} goes to the dihedrals	Meroueh and Hase (2002)
Gly-H^+ , $\text{gly}_2\text{-H}^+$	Shattering fragmentation in collisions with a diamond surface. The shattering contribution to the dissociation increases with E_i	Meroueh et al. (2002) Wang et al. (2003b)
Gly-H^+ , $\text{gly}_2\text{-H}^+$	Amber and AM1 potentials for the peptide give the same energy transfer efficiencies	Meroueh et al. (2002) Wang et al. (2003b)
$\text{Gly}_2\text{-H}^+$, $\text{ala}_2\text{-H}^+$	These two peptides have similar energy transfer efficiencies	Wang et al. (2003a)

^aThe results are for extended $\text{gly}_3\text{-H}^+$.

an interpretation of SID experiments and fundamental insight into SID energy transfer and fragmentation dynamics. The dynamics found from the simulations are reviewed in the following.

11.4.2.1. Comparison with Experiments. Excellent agreement is found between experiments and the simulations. Plots of the distributions of energy transferred to the projectile's internal degrees of freedom $P(\Delta E_{\text{int}})$ and the surface vibrations $P(\Delta E_{\text{surf}})$ and the energy remaining in the peptide translation $P(E_f)$ are given in Figure 11.13 for simulations of $\text{Cr}^+(\text{CO})_6$ collisions with the diamond {111} and

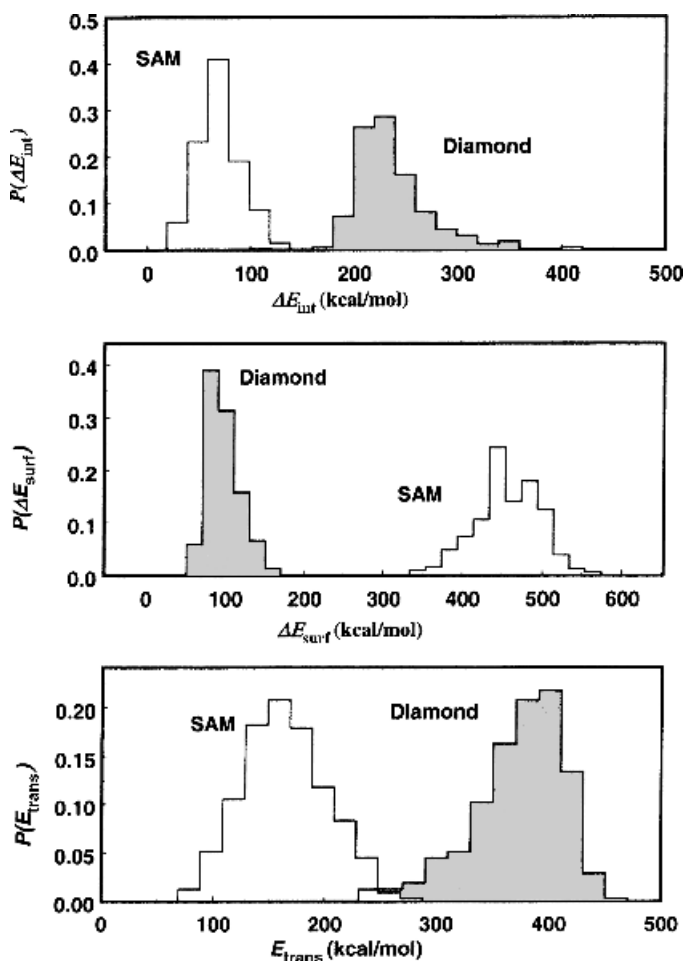


FIGURE 11.13. Distribution of energy transfer to the ion (ΔE_{int}), energy transfer to the surface (ΔE_{surf}), and the translational energy of the recoiling ion (E_f) as a result of $\text{Cr}^+(\text{CO})_6$ collisions with the diamond {111} and H-SAM surfaces at an initial translational energy of 30 eV (692 kcal/mol) and θ_i of 45° . [Reprinted with permission from Meroueh and Hase (2001).]

n-hexylthiolate H-SAM surfaces at an incident collision energy and angle of $E_i = 30$ eV and $\theta_i = 45^\circ$ (Meroueh and Hase 2001). The average energy transfer to ΔE_{int} for collision with the H-SAM is 10%, which agrees well with the value of 11–12% reported by Cooks and coworkers (Morris et al. 1992).

An indirect comparison may be made between the simulations and experiments for peptide- H^+ SID (Laskin et al. 2000; Laskin and Futrell 2003a). Laskin and coworkers find that, for collisions of $\text{ala}_2\text{-H}^+$ and the protonated octapeptide des-Arg¹-bradykinin with a fluorinated F-SAM surface at $\theta_i = 0^\circ$, the percent energy transfer to ΔE_{int} is independent of E_i for the respective ranges of 3–23 eV and 10–55 eV. For collisions of the octapeptide with diamond {111}, the energy transfer to ΔE_{int} is 19.2% and a similar value is expected for $\text{ala}_2\text{-H}^+$, since the octapeptide and $\text{ala}_2\text{-H}^+$ have similar energy transfer efficiencies when colliding with the F-SAM. Simulations have shown that energy transfer for $\text{ala}_2\text{-H}^+$ and $\text{gly}_2\text{-H}^+$ are statistically the same (Wang et al. 2003a). From this work, the suggested value for energy transfer to ΔE_{int} for $\text{ala}_2\text{-H}^+$ + diamond {111} collisions is 24% at $E_i = 30$ eV and $\theta_i = 0^\circ$. This value is close to that suggested by the above experiments.

11.4.2.2. Amber and AM1 Models for the Peptide- H^+ Intramolecular Potential. Energy transfer efficiencies given by the Amber and AM1 models for the peptide- H^+ intramolecular potential were compared in simulations of gly-H^+ and $\text{gly}_2\text{-H}^+$ collisions with the diamond {111} surface. The results are given in Table 11.7, and it is seen that there is excellent agreement between the Amber and AM1 results. In Section 11.3, the Amber potential is used to investigate the energy transfer dynamics, since the chemical dynamics simulations are much faster using Amber instead of AM1 for the peptide- H^+ intramolecular potential. The AM1 potential is used to study the fragmentation dynamics in Section 11.4.

TABLE 11.7. Comparison of Amber and AM1 Peptide- H^+ Intramolecular Potentials for Simulations of Energy Transfer in SID

Potential	Average Percent Energy Transfer ^a		
	ΔE_{int}	ΔE_{surf}	E_f
Gly- H^+ , $E_i = 70$ eV and $\theta_i = 45^\circ$			
AMBER	11	37	52
AM1	12	38	50
Gly ₂ - H^+ , $E_i = 70$ eV and $\theta_i = 45^\circ$			
AMBER	15	25	60
AM1	13	26	61
Gly ₂ - H^+ , $E_i = 70$ eV and $\theta_i = 0^\circ$			
AMBER	20	40	40
AM1	20	40	40

^aThe standard deviation of the mean for the percent energy transfer is of the order of 1%.

11.4.2.3. Energy Transfer Dynamics

11.4.2.3.1. Pathways for Energy Transfer. It is important to know which modes of the projectile are initially excited when it collides with the surface. Such a property is discussed above, in Section 11.3.2.2.6 for Ar^+ peptide- H^+ collisions. The simulations of $\text{Cr}^+(\text{CO})_6$ collisions with the diamond {111} and *n*-hexyl thiolate H-SAM surfaces show there is very little energy transfer to the CO vibrations during the collision of $\text{Cr}^+(\text{CO})_6$ with the surface or later, as a result of intramolecular vibrational energy redistribution (IVR), after the ion scatters off the surface (Song et al. 2003). Thus, of the ion's 33 vibration degrees of freedom, 6 are apparently inactive. The inactivity of the CO vibrations for receiving and transferring energy is not unexpected, given their high frequencies and the much lower frequencies for the remaining $\text{Cr}^+(\text{CO})_6$ vibrations. No attempt was made to determine which modes of the $\text{Cr}^+(\text{CO})_6$ ion are initially excited on its impact with the surface.

A simulation was performed for folded $\text{gly}_3\text{-H}^+$ collisions with diamond {111}, similar to the $\text{Ar} + \text{gly}_4\text{-H}^+$ simulation discussed above, where modes of $\text{gly}_4\text{-H}^+$ are constrained to determine the pathways for collisional excitation of the peptide. With none of the modes of $\text{gly}_3\text{-H}^+$ constrained, 18, 9, and 73% of $E_i = 30$ eV, for $\theta_i = 45^\circ$ collisions, is transferred to E_{int} , E_{surf} , and E_{f} . With all the modes of the $\text{gly}_3\text{-H}^+$ peptide constrained, except the dihedrals, the respective energy transfers are 14%, 16%, and 70%. This result suggests that $\frac{14}{18} \times 100 = 78\%$ of the internal energy transfer is to the peptide dihedrals, a result similar to that found for $\text{Ar} + \text{gly}_4\text{-H}^+$ collisions.

11.4.2.3.2. Surface Properties. The simulations show that the properties of the surface have a profound effect on the energy transfer efficiencies. This is illustrated in Table 11.8 for collisions of $\text{Cr}^+(\text{CO})_6$ and folded $\text{gly}_3\text{-H}^+$ with the diamond {111}

TABLE 11.8. Comparisons of Trajectory Simulations of Energy Transfer (%) for Folded $\text{Gly}_3\text{-H}^+$ and $\text{Cr}^+(\text{CO})_6$ Collisions with Diamond {111} and H-SAM Surfaces^a

E_i^b	ΔE_{int}		ΔE_{surf}		E_{f}	
	(Gly) ₃	$\text{Cr}(\text{CO})_6^+$	(Gly) ₃	$\text{Cr}(\text{CO})_6^+$	(Gly) ₃	$\text{Cr}(\text{CO})_6^+$
<i>Diamond {111}</i>						
30	18	30	9	14	73	56
70	17	17	21	29	62	54
110	14	16	29	38	57	46
<i>H-SAM^c</i>						
30	7	10	63	69	30	21
70	—	9	—	81	—	10
110	—	8	—	81	—	11

^aThe collision angle is 45° .

^bThe collision energy is in eV.

^cThe H-SAM is *n*-hexyl thiolate.

and *n*-hexyl thiolate H-SAM surfaces. Collision with diamond {111} transfers a factor of 2–3 more energy to ΔE_{int} as compared to colliding with the H-SAM. Collisions with the diamond {111} surface retain the majority of the collision energy in projectile translation, while collisions with the H-SAM deposit the majority of the energy in ΔE_{surf} . These results concur with the experiments (Laskin and Futrell 2003a), which show that for collisions of the singly protonated octapeptide des-Arg¹-bradykinin with different surfaces the percent $E_i \rightarrow \Delta E_{\text{int}}$ transfer increases in the order H-SAM (10%), LiF (12.0%), diamond (19.2%), and F-SAM (20.5%).

Another important difference between collisions with the diamond {111} and H-SAM surfaces is the greater breadth of the $P(\Delta E_{\text{int}})$ distribution for collision with diamond {111}. This is illustrated in Figure 11.13 for $\text{Cr}^+(\text{CO})_6$ collision, at 30 eV. At the higher E_i of 70 and 110 eV, $P(\Delta E_{\text{int}})$ appears to become bimodal (Song et al. 2003). A broader $P(\Delta E_{\text{int}})$ for collision with the diamond {111} surface, is also seen for peptide- H^+ projectiles, as shown in Figure 11.14 for folded $\text{gly}_3\text{-H}^+$.

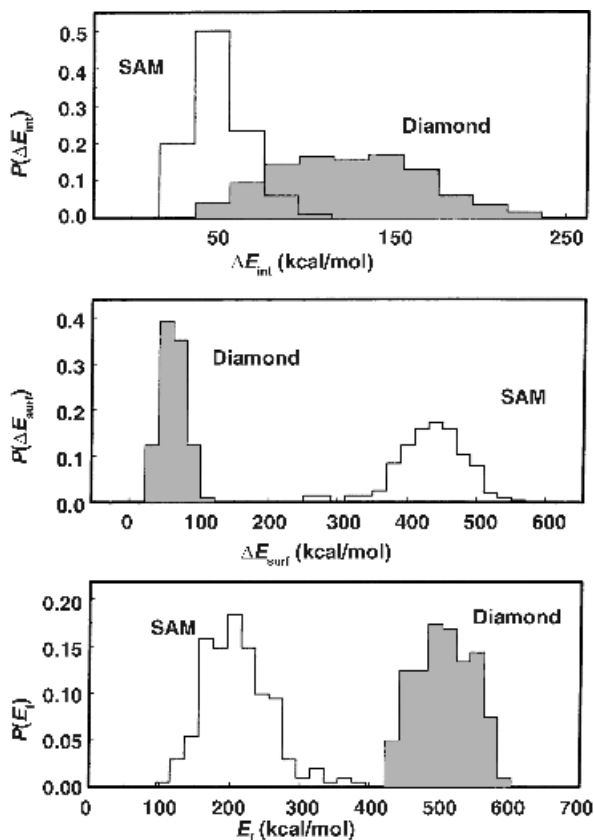


FIGURE 11.14. Distribution of the energy transfer to the ion (ΔE_{int}) and to the surface (ΔE_{surf}) and the translational energy of the recoiling ion (E_f) following folded $\text{gly}_3\text{-H}^+$ collisions with diamond and H-SAM surfaces at an initial translational energy of 30 eV (692 kcal/mol) and θ_i of 45° . [Reprinted with permission from Meroueh and Hase (2002).]

The origin of the difference in the energy transfer dynamics for collisions with the diamond and H-SAM surfaces is unclear. It has been suggested from simulations that the stiffness of the diamond {111} surface enhances energy transfer to the projectile ion (Meroueh and Hase 2001). From experiments (Laskin and Futrell 2003a) it has been inferred that the surface stiffness has a major effect on the width of $P(\Delta E_{\text{int}})$, while the average energy deposited into the ion is affected mainly by the mass of the chemical moiety representing an immediate collision partner for the ion impacting the surface. The interpretation of the experiments is similar to that of the simulations, since the effective mass of the surface impact site depends on the surface stiffness (Grimmelmann et al. 1980; de Sainte Claire et al. 1995).

11.4.2.3.3. Peptide Size, Structure, and Amino Acid Constituents. An important finding is that the size, structure, and amino acid constituents of the peptide- H^+ ions do not have substantial effects on the energy transfer efficiencies. For collision with diamond {111} at $E_i = 30$ eV and $\theta_i = 45^\circ$, the respective energy transfer to ΔE_{int} , ΔE_{surf} , and E_f are 18%, 9%, and 73% for $\text{gly}_3\text{-H}^+$ and 23%, 5%, and 72% for $\text{gly}_5\text{-H}^+$, (Meroueh and Hase 2002). For $E_i = 70$ eV and $\theta_i = 45^\circ$, and collision with the diamond surface, the transfer to ΔE_{int} is 11%, 15%, and 17% for gly-H^+ , $\text{gly}_2\text{-H}^+$, and $\text{gly}_3\text{-H}^+$, respectively (Wang et al. 2003a). The energy transfer to ΔE_{int} is similar for these different size $\text{gly}_n\text{-H}^+$ peptides.

The structure of the peptide has at most only a small effect on the energy transfer. For collisions with diamond at $E_i = 30$ eV and $\theta_i = 45^\circ$, the transfer to ΔE_{int} is 18%, and 20%, respectively, for folded and extended $\text{gly}_3\text{-H}^+$. For collision with the n-hexyl thiolate H-SAM, these respective energy transfers are 7%, and 8%. Thus variations in the structure of the peptide have an insignificant effect on the energy transfer. Energy transfer has been studied for both $\text{gly}_n\text{-H}^+$ and $\text{ala}_n\text{-H}^+$ peptides, and, for the same n , both peptides have similar energy transfer efficiencies (Wang et al. 2003a). Thus, alanine and glycine constituents are equally efficient in receiving energy.

The independence of the energy transfer on peptide size, observed in the simulations and amino acid constituents, agrees with experimental results (Laskin and Futrell 2003a). For $\text{ala}_2\text{-H}^+$ collisions with a F-SAM surface 21% of E_i is transferred to ΔE_{int} , while this transfer is 20.5% for des-Arg¹-bradykinin collisions with the same surface.

11.4.2.3.4. Projectile Incident Energy and Angle. Experimental studies of $\text{ala}_2\text{-H}^+$ SID on a F-FAM surface for E_i in the range of 2–23 eV (Laskin et al. 2000) and protonated des-Arg¹-bradykinin SID on a variety of surfaces for E_i in the range of 10–100 eV (Laskin and Futrell 2003a) have shown that the percent energy transfer to ΔE_{int} is independent of E_i . A similar result is found from the simulation. For $\text{gly}_2\text{-H}^+$ SID at $\theta_i = 45^\circ$, the percent energy transfer to ΔE_{int} changes from 16 to 13% as E_i is increased from 5 to 110 eV (Wang et al. 2003a). For $\text{ala}_2\text{-H}^+$ the energy transfer changes from 19 to 15%. These small changes in the transfer to ΔE_{int} , over a large range of E_i , may be difficult to observe experimentally.

There are changes in the energy transfer efficiencies with change in collision angle. This is illustrated in Table 11.7 for $\text{gly}_2\text{-H}^+$ collisions with the diamond

surface. There is a small increase in the percent transfer to ΔE_{int} as θ_i is changed from 45° to 0° . In contrast, the change in the projectile translation energy is much larger, decreasing from 60 to 40%.

11.4.2.3.5. Projectile Orientation and Surface Impact Site. Simulations of $\text{gly}_2\text{-H}^+$ colliding with the diamond {111} surface, at E_i of 70 eV and θ_i of 0° and 45° , were performed to determine how the orientation angle of the peptide ion and the surface impact site affect the collisional energy transfer (Rahaman et al. 2006). The peptide ion was randomly rotated in the trajectory initial conditions, which establishes the initial orientation of the ion with respect to the surface. To ensure the peptide ion approaches the surface in this orientation, the rotational temperature of the ion was set to 0 K. The initial orientation of the peptide ion is determined by defining a vector from the nitrogen atom of the protonated amino group to the hydroxyl oxygen atom of the carboxylic group. The angle between this vector and the vector normal to the diamond surface determines the orientation of the peptide ion. There are two unique impact sites on the diamond {111} surface at which the center of mass of $\text{gly}_2\text{-H}^+$ may collide. One is a hydrogen atom on the outer layer of the surface. The other is a carbon atom in the second surface layer that is bonded to a carbon atom just below the surface hydrogen atom. The first impact site is denoted a H site and second, a C site. In order to determine possible effects of the surface impact point on the efficiency of energy transfer to $\text{gly}_2\text{-H}^+$, one ensemble of classical trajectories was calculated with the center of mass of the diglycine ion directed toward the H site and another with the ion directed towards the C site. An ensemble of trajectories was also calculated with random impact sites for the colliding ion. The results of the simulations are shown in Figure 11.15.

The top graphs in the figure show that the energy transfer to ΔE_{int} is independent of the impact site. The same is found for the $P(\Delta E_{\text{surf}})$ and $P(E_f)$ distributions, which are not shown. However, the middle graphs show that energy transfer to ΔE_{int} is enhanced if the backbone of the peptide is perpendicular to the surface during the collision. Concurrently, the transfer to ΔE_{surf} and the energy remaining in projectile translation are decreased for the perpendicular orientation. For these perpendicular collisions, more energy is transferred to the peptide if the C terminus ($\Psi = 180^\circ$) instead of the N terminus first strikes the surface. For an incident angle θ_i of 45° , instead of 0° , the role of peptide orientation on the energy transfer efficiency is less pronounced. This is shown in the bottom graphs in Figure 11.15.

11.4.2.4. Fragmentation Mechanisms. Simulations for $\text{Cr}^+(\text{CO})_6$, gly-H^+ , and $\text{gly}_2\text{-H}^+$ show that the projectile ion may fragment by two different mechanisms (Meroueh and Hase 2001; Song et al. 2003, Meroueh et al. 2002; Wang et al. 2003b). One is the traditional RRKM model in which the projectile ion is activated by collision with the surface, “bounces off”, and then dissociates after undergoing intramolecular vibrational energy redistribution (IVR). The other mechanism is shattering, which dominates at high collision energy. For shattering the ion fragments as it collides with the surface (Raz and Levine 1996).

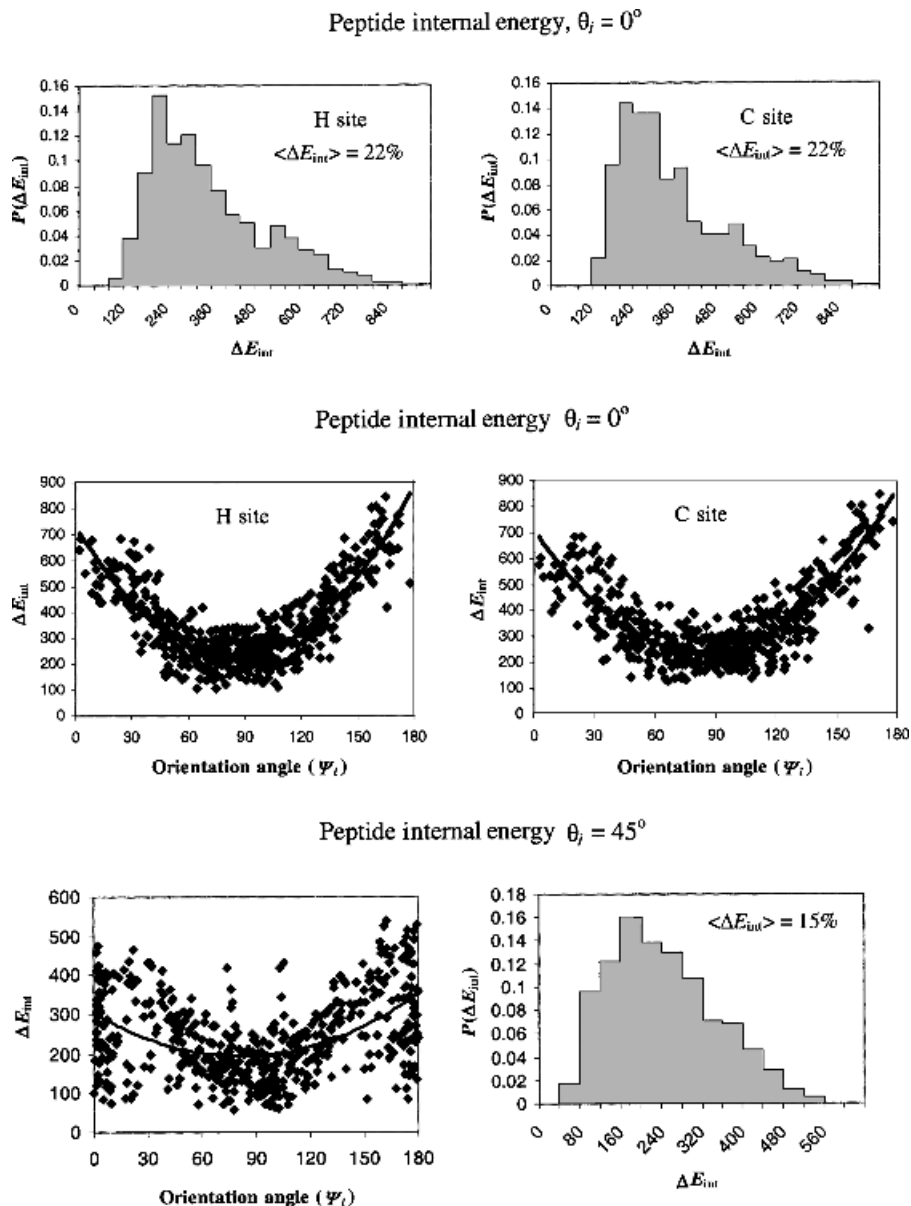


FIGURE 11.15. Upper graphs: distributions of ΔE_{int} for $\text{gly}_2\text{-H}^+$ collisions with the H-atom and C-atom sites of diamond {111}. Energy in the plots is in kcal/mol. $E_i = 70$ eV and $\theta_i = 0^\circ$. Middle graphs: scatterplots of the energy transfers in the upper plots, versus the $\text{gly}_2\text{-H}^+$ orientation angle. The curves are parabolic fits. Energy in the plots is in kcal/mol. Lower graphs: simulation results for $E_i = 70$ eV and $\theta_i = 45^\circ$. Both energy transfer distributions and scatter-plots of the energy transfer versus $\text{gly}_2\text{-H}^+$ orientation angle are given. Energy in the plots is in kcal/mol. [Reprinted with permission from Rahaman et al. (2006).]

11.4.2.4.1. $\text{Cr}^+(\text{CO})_6$ Dissociation. Shattering is observed in collisions of $\text{Cr}^+(\text{CO})_6$ with the diamond {111} surface at E_i of 30, 70, and 110 eV (Song et al. 2003). For $E_i = 30$ eV, the $n = 4-6$ $\text{Cr}^+(\text{CO})_n$ ions dissociate by shattering, while the dissociation for $n = 1-3$ is RRKM-like. For $E_i = 70$ eV, the $n = 4-6$ dissociate by shattering, the dissociation of the $n = 1, 2$ ions is RRKM-like, and the dissociation of $n = 3$ ions exhibits a transition from shattering to RRKM behavior. At the highest E_i studied of 110 eV, each of the $n = 4-6$ ions and the majority of the $n = 1-3$ ions dissociate by shattering. The importance of shattering is illustrated in Figure 11.16, where scatterplots are given of the height (h) of the ion above the surface at the time dissociation occurred versus the ion's dissociation lifetime (τ).

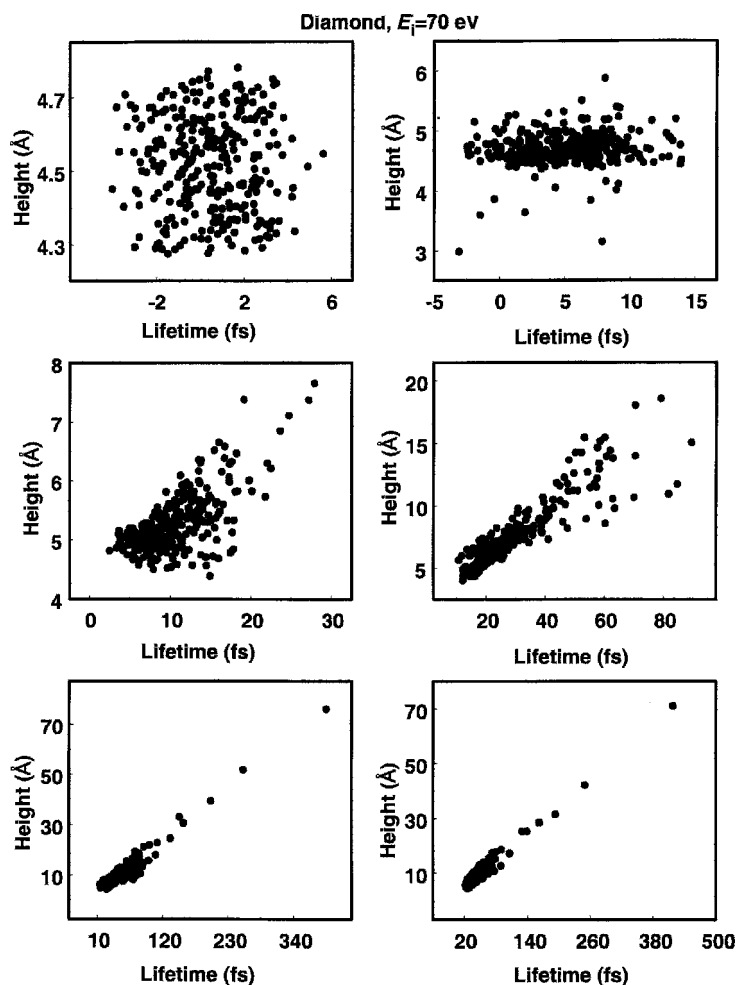


FIGURE 11.16. Scatterplots of the height of the $\text{Cr}^+(\text{CO})_n$ ions above the diamond {111} surface when $\text{Cr}^+(\text{CO})_n \rightarrow \text{Cr}^+(\text{CO})_{n-1} + \text{CO}$ dissociation occurs versus the dissociation lifetime. Results are for $E_i = 70$ eV and $\theta_i = 45^\circ$. The H atoms define the top of the diamond surface. [Reprinted with permission from Song et al. (2003).]

For $\text{Cr}^+(\text{CO})_6$ collision with a H-SAM surface, at $\theta_i = 45^\circ$ and E_i of 30 and 70 eV, there is no shattering and dissociation of each of the $\text{Cr}^+(\text{CO})_n$ ions is RRKM-like. However, at the higher collision energy 110 eV, the $n = 4-6$ ions dissociate by shattering, with some shattering also for the $n = 3$ ions. Dissociation of the $n = 1, 2$ ions remains RRKM-like. For some of the collisions with the H-SAM, at E_i of both 70 and 110 eV, the dissociations occur at heights of zero or less and thus occur while the ion has penetrated the surface.

Shattering requires direct $T \rightarrow V$ energy transfer into the rupturing Cr^+-CO bond(s) as $\text{Cr}^+(\text{CO})_6$ impacts the surface. The probability of this energy transfer is expected to increase as the collision energy E_i is increased and this is the observed result. The greater likelihood of shattering for collisions with the hard diamond, as compared to the softer H-SAM surface, is greater with more efficient $T \rightarrow V$ energy transfer for collision with the diamond surface. That some collisions lead to shattering and others to RRKM-like dissociation, for a fixed E_i , may result from the orientation of $\text{Cr}^+(\text{CO})_6$ as it impacts the surface. This possible effect should be investigated in future work. It may be related to the near bimodal $P(\Delta E_{\text{int}})$ distribution observed for $\text{Cr}^+(\text{CO})_6$ collisions with diamond (Song et al. 2003).

11.4.2.4.2. Gly- H^+ and Gly₂- H^+ Dissociation. The AM1 semiempirical model for the peptide- H^+ intramolecular potential was used to study the fragmentation mechanism for gly- H^+ and gly₂- H^+ dissociation (Meroueh et al. 2002; Wang et al. 2003b). The diamond {111} surface was used for these simulations. For gly- H^+ + diamond {111}, at $E_i = 70$ eV and $\theta_i = 45^\circ$, 23% of the collisions resulted in fragmentation by shattering. Within the 1.5 ps of the trajectories, another 19% dissociated by IVR and a RRKM-like mechanism; 58% of the trajectories did not dissociate during the timescale of the simulation. The SID fragmentation dynamics of gly₂- H^+ + diamond {111} collisions was simulated at E_i of 30, 50, 70, and 100 eV for $\theta_i = 0^\circ$, perpendicular collisions. The trajectories were only integrated for a maximum time of 1 ps and not all the trajectories fragmented. The percent that fragmented increased with E_i and were 21%, 44%, 66%, and 83% for E_i of 30, 50, 70, and 100 eV, respectively. The fragmenting trajectories were analyzed to determine the site where the initial bond rupture occurred. These sites are identified by the lettering scheme in Figure 11.17.

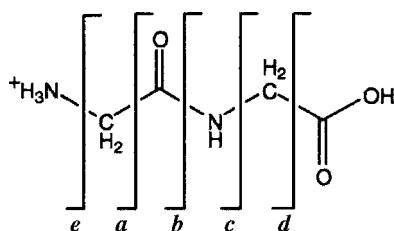


FIGURE 11.17. Possible initial bond rupture sites, leading to fragmentation, for gly₂- H^+ . [Reprinted with permission from Wang et al. (2003b).]

TABLE 11.9. Fraction of Gly₂-H⁺ + Diamond {111} Fragmentation Occurring by Different Initial Bond Ruptures^a

E_i^b	Number of Trajectories	Fragmenting Fraction ^c	Fragmentation Fraction Initiated at Different Bond Rupture Sites				
			<i>a</i>	<i>b</i>	<i>c</i>	<i>d</i>	<i>e</i>
30	100	0.21	0.18	0.02	0	0	0.01
50	100	0.44	0.31	0.01	0	0.06	0.06
70	122	0.66	0.43	0.12	0	0.09	0.02
100	106	0.83	0.56	0.03	0	0.15	0.09

^aThe initial bond rupture sites are shown in Figure 11.17.^b E_i is in units of eV.^cNumber of trajectories that fragment divided by the total number of trajectories.

The number of trajectories calculated at each E_i and the fraction of the fragmentation occurring by the different initial bond rupture sites are given in Table 11.9. The fraction of the gly₂-H⁺ trajectories that dissociate increases with increase in E_i . Site *a* is the most probable position for initial bond rupture to occur, increasing to 56% for $E_i = 100$ eV. In addition, there is no initial bond rupture at site *c*. The absence of dissociation at site *c* is consistent with previous experimental (Klassen and Kebarle 1997) and computational (Paizs and Suhai 2001; Yalcin et al. 1995) studies for diglycine fragmentation. Preference for initial bond rupture at site *a*, namely, the CH₂-CONH bond, concurs with the fragmentation mechanism proposed (Paizs and Suhai 2001) for which the initial step is elimination of CO bonded to the amide nitrogen. As found from CID experiments (Klassen and Kebarle 1997), the ions NH₂CH₂⁺ and its isomer NH₃CH₂⁺ are principal fragmentation products.

The number of product channels observed in the gly₂-H⁺ + diamond {111} simulations increases dramatically as E_i is increased; 6, 23, 44, and 59 different product channels are observed for E_i of 30, 50, 70, and 100 eV, respectively. This increase in the number of product channels is a result of shattering, in which dissociation occurs as gly₂-H⁺ collides with the surface. The shattering results are summarized in Table 11.10, where the fraction of the trajectories that shatter is listed

TABLE 11.10. Fraction of Gly₂-H⁺ + Diamond {111} Trajectories that Fragment by Shattering

E_i^a	Shattering Fraction ^b	Shattering Fraction Initiated at Different Bond Rupture Sites				
		<i>a</i>	<i>b</i>	<i>c</i>	<i>d</i>	<i>e</i>
30	0.08	0.06	0.02	0	0	0
50	0.13	0.10	0	0	0	0.03
70	0.44	0.29	0.08	0	0.06	0.01
100	0.71	0.48	0.02	0	0.13	0.08

^aCollision energy in eV.^bNumber of trajectories that shatter divided by the total number of trajectories.

as well as the fraction that shatter for the different initial bond rupture sites: sites *a*, *b*, *c*, *d*, and *e* in Figure 11.17. The fraction of the trajectories that shatter increases from 0.08 to 0.71 as E_i is increased from 30 to 100 eV. For all E_i the most important initial bond rupture site for shattering is site *a*. At low E_i of 30 and 50 eV shattering is also observed with initial dissociation at sites *b* and *e*. Shattering occurs with initial dissociation at site *d* for E_i of 70 eV and this becomes the second most important initial dissociation site for shattering at E_i of 100 eV.

At each E_i the principal product channels are those with initial rupture of site *a* in Figure 11.17 and formation of the immonium ion NH_2CH_2^+ . Initial rupture at site *a* and formation of NH_2CH_2^+ constitute 81%, 36%, 35%, and 11% of the fragmentation channels at E_i of 30, 50, 70, and 100 eV, respectively. The decrease in the yield of this ion as E_i is increased, results from the onset of the multitude of shattering pathways. From experiments (Klassen and Kebarle 1997), NH_2CH_2^+ is expected to be the principal product ion in CID.

The energy transfer efficiencies of E_f , ΔE_{int} , and ΔE_{surf} are very similar for shattering and nonshattering trajectories, and shattering is not concomitant with a significantly larger transfer of ΔE_{int} than for nonshattering events. Initial studies suggest that shattering is influenced by the orientation of $\text{gly}_2\text{-H}^+$ as it collides with the surface. This is consistent with a suggestion (Meroueh et al. 2002) that shattering is promoted by collisions that direct $\text{gly}_2\text{-H}^+$ to a dissociation transition state on impact with the surface. An incomplete analysis (Wang et al. 2003b) suggests shattering is enhanced when the peptide chain is oriented perpendicular to the surface during collision, so that one “end” of the chain first strikes the surface. A number of important questions may be addressed by an analysis of peptide- H^+ orientation and shattering in the simulations. What fraction of ions has the proper orientation to decompose by a shattering mechanism? Does orientation select particular transition states? How do the shattering transition states differ from transition states involved in RRKM type dissociation?

11.4.2.4.3. Peptide- H^+ Shattering in Simulation and Experiments. The simulations presented above illustrate the importance of shattering for gly-H^+ and $\text{gly}_2\text{-H}^+$ SID during collisions with the diamond {111} surface. Shattering is exemplified by many product channels and the relative product yields for these channels are unrelated to their dissociation thresholds; thus, an RRKM analysis does not predict the presence of such a large number of dissociation channels, nor the observed relative product yields. Shattering becomes increasingly important as E_i is increased.

From experimental studies (Laskin et al. 2003; Laskin and Futrell 2003b,c) of des-Arg¹- and des-Arg⁹-bradykinin and fibrinopeptide SID, shattering has been suggested for high-energy collisions. As in the simulations, shattering becomes more important as the collision energy is increased and the appearance of many more product channels, than predicted by unimolecular thresholds and RRKM theory is attributed to shattering. The dissociation of peptide- H^+ ions in the experiments may be modeled by two decay rates (slow and fast), with the later modeled by the “sudden death” approximation, in which the molecule fragments instantaneously if its internal energy reaches a certain threshold. It is stated (Laskin

and Futrell 2003b) that “instantaneous fragmentation of large molecules at high collision energies occurs on or very near the surface rather than in the gas phase and indicates a transition in the dynamics of ion–surface interaction—namely, the shattering transition.” This is the picture of the shattering dynamics observed in the simulations.

An unresolved issue in comparing the simulation and experimental studies of shattering is that in the experiments the ions are observed on a 1 ms or larger timescale. Additional information needed, to compare with experiment, are the translational energies of ions formed by shattering. This will be determined in future simulations.

11.5. FUTURE DIRECTIONS

The presentations and discussions in this chapter show that classical trajectory chemical dynamics simulations give accurate results for the atomic-level details of CID and SID. They may be used to study the dynamics of both the energy transfer and unimolecular dissociation processes, and may be compared directly with experiment. They also provide the fundamental information needed to develop accurate theoretical models for CID and SID.

Although much has been achieved from the simulations, a considerable amount of additional work needs to be done. To date only the SID of protonated peptides with alanine and glycine constituents have been simulated, and it is important to consider additional polypeptides with a variety of amino acids. Also, different surfaces need to be investigated. The reported simulation results are for diamond and H-SAM surfaces, while experiments have also considered surfaces with varying degrees of fluorination and hydroxylation (Smith et al. 2002, 2003). It would also be of interest to consider organic surfaces with additional types of functionalization (Ferguson et al. 2004).

For the potential energy surfaces used in the simulations, the intermolecular potentials between the projectile ions and surfaces have been represented by analytic functions fit to *ab initio* calculations. Furthermore, these fits have focused on the short-range repulsive regions of the intermolecular potential, so that the energy transfer during the projectile’s initial impact with the surface is correctly described. These models do not accurately represent the projectile–surface attractive interaction, nor represent possible projectile + surface chemical reactions. The inaccurate attractive potentials preclude the possibility of simulating soft-landing experiments (Miller et al. 1997), in which projectile ions are captured intact on either solid or liquid surfaces. Soft landing may be simulated by fitting analytic potential energy functions to high-level *ab initio* calculations that give accurate representations of both the short-range and long-range regions of the intermolecular potentials (Yan and Hase 2002). Chemical reaction between the projectile and the surface may be simulated by QM/MM direct dynamics trajectory calculations in which the potential energy for the projectile and the projectile’s interaction with the surface are represented by a quantum mechanics (QM) electronic structure theory (Li et al. 2000). In the simulation only the part of the surface directly interacting with

the projectile is represented by the QM model. The remaining surface atoms are represented by analytic molecular mechanics (MM) potentials, with a QM/MM interface connecting the QM and MM surface regions.

The previous direct dynamics simulations of peptide- H^+ surface collisions have used QM+MM models, in which the peptide- H^+ potential is the semiempirical AM1 QM model and the peptide- H^+ /surface and surface potentials are analytic MM-type potentials. These QM+MM models do not allow reaction with the surface. Only the gly- H^+ and gly₂- H^+ peptides have been considered in these simulations and it is important to extend these simulations to larger peptides with a range of amino acid constituents. In addition, higher level QM methods such as MP2 and DFT need to be investigated. It is important to determine if these more accurate QM models also show that shattering is an important peptide- H^+ fragmentation mechanisms. The MP2 and DFT models may also be used in the QM/MM studies of peptide- H^+ + surface collisions, from which both shattering and reaction with the surface may be investigated.

ACKNOWLEDGMENTS

The authors' CID and SID simulations were supported by the National Science Foundation. Special thanks are expressed to Jean Futrell, Julia Laskin, and Vicki Wysocki for valuable discussions concerning the dynamics of peptide- H^+ SID.

REFERENCES

- Allen MP, Tildesley DJ (1987): *Computer Simulation of Liquids*, Oxford, New York.
- Baer T, Hase WL (1996): *Unimolecular Reaction Dynamics—Theory and Experiments*, Oxford Univ. Press, New York.
- Blais NC, Bunker DL (1962): Monte Carlo calculations. II. The reactions of alkali atoms with methyl iodide. *J. Chem. Phys.* **37**:2713–2720.
- Bolton K, Hase WL, Peslherbe GH (1998): Direct dynamics simulations of reactive systems. In Thompson DL (ed), *Modern Methods for Multidimensional Dynamics Computations in Chemistry*, World Scientific, London, pp. 143–189.
- Bolton K, Hase WL (1998): Integrating the classical equations of motion. In Allinger NL (ed), *Encyclopedia of Computational Chemistry*, Vol. 2, Wiley, New York, pp. 1347–1360.
- Bosio SBM, Hase WL (1997): Energy transfer in rare gas atom collisions with self-assembled monolayers. *J. Chem. Phys.* **107**:9677–9686.
- Bosio SBM, Hase WL (1998): Simulations of energy transfer in $\text{Cr}^+(\text{CO})_6$ surface induced dissociation. *Int. J. Mass Spectrom. Ion Proc.* **174**:1–9.
- Bunker DL (1962): Monte Carlo calculations of triatomic dissociation rates. I. N_2O and O_3 . *J. Chem. Phys.* **37**:393–403.
- Bunker DL, Goring-Simpson EA (1973): Alkali-methyl iodide reactions. *Faraday Discuss. Chem. Soc.* **55**:93–99.
- Bunker DL, Chapman S (1975): An exploratory study of reactant vibrational effects in $\text{CH}_3 + \text{H}_2$ and its isotopic variants. *J. Chem. Phys.* **66**:1523–1533.

- Califano S (1976): *Vibrational States*, Wiley, New York.
- Cornell WD, Cieplak P, Bayley CI, Gould IR, Merz KM, Ferguson DM, Spellmeyer DC, Fox T, Cladwell JW, Kollman PA (1995): A second generation force field for the simulation of proteins, nucleic acids, and organic molecules. *J. Am. Chem. Soc.* **117**:5179–5197.
- de Sainte Claire P, Hase WL (1996): Thresholds for the collision-induced dissociation of clusters by rare gas impact. *J. Phys. Chem.* **100**:8190–8196.
- de Sainte Claire P, Peslherbe GH, Hase WL (1995): Energy transfer dynamics in the collision-induced dissociation of Al_6 and Al_{13} clusters. *J. Phys. Chem.* **99**:8147–8161.
- Dewar MJS, Zoebisch EG, Healy EF, Stewart JJP (1985): The development and use of quantum mechanical molecular models. 76. AM1: A new general purpose quantum mechanical molecular model. *J. Am. Chem. Soc.* **107**:3902–3909.
- Ferguson MK, Lohr JR, Day BS, Morris JR (2004): Influence of buried hydrogen-bonding groups within monolayer films on gas-surface energy exchange and accommodation. *Phys. Rev. Lett.* **92**:073201.
- Frisch MJ, Head-Gordon M, Pople JA (1988): A direct MP2 gradient method. *Chem. Phys. Lett.* **166**:275–280.
- Goldstein H (1950): *Classical Mechanics*, Addison-Wesley, London.
- Granucci G, Toniolo A (2000): Molecular gradients for semiempirical CU wavefunctions with floating occupation molecular orbitals. *Chem. Phys. Lett.* **325**:79–85.
- Grebenschikov SY, Schinke R, Hase WL (2003). State-specific dynamics of unimolecular dissociation. In Green NJB (ed), *Comprehensive Chemical Kinetics*, Vol. 39, *Unimolecular Kinetics*, Part 1. *The Reaction Step*, Elsevier, New York, pp. 105–242.
- Grimmelmann EK, Tully JC, Cardillo MJ (1980): Hard-cube model analysis of gas-surface energy accommodation. *J. Chem. Phys.* **72**:1039–1043.
- Hanley L, Ruatta SA, Anderson SL (1987): Collision-induced dissociation of aluminum cluster ions: Fragmentation patterns, bond energies, and structures for Al_2^+ – Al_7^+ . *J. Chem. Phys.* **87**:260–268.
- Hariharan PC, Pople JA (1973): Influence of polarization on MO hydrogenation energies. *Theor. Chim. Acta* **28**:213–222.
- Hariharan PC, Pople JA (1974): Accuracy of AH_n equilibrium geometries by single determinant molecular orbital theory. *Mol. Phys.* **1**:209–214.
- Hase WL (ed), (1998a): *Advances in Classical Trajectory Methods*, Vol. 3, *Comparisons of Classical and Quantum Dynamics*. JAI Press, London.
- Hase WL (1998b): Classical trajectory simulations: Final conditions. In Allinger NL (ed), *Encyclopedia of Computational Chemistry*, Vol. 1, Wiley, New York, pp. 399–402.
- Hase WL (1998c): Classical trajectory simulations: Initial conditions. In Allinger NL (ed), *Encyclopedia of Computational Chemistry* Vol. 1, Wiley, New York, pp. 402–407.
- Hase WL, Buckowski DG (1982): Dynamics of ethyl radical decomposition. II. Applicability of classical mechanics to large molecule unimolecular reaction dynamics. *J. Comput. Chem.* **3**:335–343.
- Hase WL, Mondro SL, Duchovic RJ, Hirst, DM (1987): Thermal rate constant for $\text{H} + \text{CH}_3 \rightarrow \text{CH}_4$ recombination. III. Comparison of experiment and canonical variational transition state theory. *J. Am. Chem. Soc.* **109**:2916–2922.
- Hase WL, Song K, Gordon MS (2003): Direct dynamics simulations. *Comput. Sci. Eng.* **5**:36–44.

- Hass KC, Tamor MA, Anthony TR, Banholzer WF (1992): Lattice dynamics and Raman spectra of isotopically mixed diamond. *Phys. Rev. B* **45**:7171–7182.
- Head-Gordon M, Pople JA, Frisch MJ (1988): MP2 energy evaluation by direct methods. *Chem. Phys. Lett.* **153**:503–506.
- Isa N, Gibson KD, Yan T-Y, Hase WL, Sibener SJ (2004): Experimental and simulation study of neon atom collision dynamics with a 1-decanthiol monolayer. *J. Chem. Phys.* **120**:2417–2433.
- Jarrold MF, Bower EJ, Krauss JS (1987): Collision-induced dissociation of metal cluster ions: Bare aluminum clusters, Al_n^+ ($n = 3-26$). *J. Chem. Phys.* **86**:3876–3885.
- Khan FA, Clemmer DE, Schultz RH, Armentrout PB (1993): Sequential bond energies of $Cr(CO)_x$, $x = 1-6$. *J. Chem. Phys.* **97**:7978–7987.
- Klassen JS, Kebarle P (1997): Collision-induced dissociation threshold energies of protonated glycine, glycineamide, and some related small peptides and peptide amino amides. *J. Am. Chem. Soc.* **119**:6552–6563.
- Laskin J, Denisov E, Futrell JH (2000): A comparative study of collision-induced and surface-induced dissociation. 1. Fragmentation of protonated dialanine. *J. Am. Chem. Soc.* **122**:9703–9714.
- Laskin J, Bailey TH, Futrell JH (2003): Shattering of peptide ions on self-assembled monolayer surface. *J. Am. Chem. Soc.* **125**:1625–1632.
- Laskin J, Futrell JH (2003a): Energy transfer in collisions of peptide ions with surfaces. *J. Chem. Phys.* **119**:3413–3420.
- Laskin J, Futrell JH (2003b): Surface-induced dissociation of peptide ions: Kinetics and dynamics. *J. Am. Soc. Mass Spectrom.* **14**:1340–1347.
- Laskin J, Futrell JH (2003c): Collisional activation of peptide ions in FT-ICR mass spectrometry. *Mass Spectrom. Rev.* **22**:158–181.
- Li G, Bosio SBM, Hase WL (2000): A QM/MM model for $O(^3P)$ reaction with an alkyl thiolate self-assembled monolayer. *J. Mol. Struct.* **556**:43–57.
- Lian L, Su C-X, Armentrout PB (1992): Collision-induced dissociation of Ni_n^+ ($n = 2-18$) with Xe: Bond energies, geometrical structures, and dissociation pathways. *J. Chem. Phys.* **96**:7542–7554.
- Liu J, Song K, Hase WL, Anderson SL (2003): Direct dynamics study of energy transfer and collision-induced dissociation: Effect of impact energy, geometry, and reactant vibrational modes in H_2CO^+-Ne collisions. *J. Chem. Phys.* **119**:3040–3050.
- Mahan BH (1970): Refined impulse approximation for the collisional excitation of the classical harmonic oscillator. *J. Chem. Phys.* **52**:5221–5225.
- Mar W, Klein M (1994): Molecular dynamics study of the self-assembled monolayer composed of $S(CH_2)_{14}CH_3$ molecules using an all-atoms model. *Langmuir* **10**:188–196.
- Martinez-Nuñez E, Fernandez-Ramos A, Vazquez SA, Marquez JMC, Xue M, Hase WL (2005): Quasiclassical dynamics simulation of the collision-induced dissociation of $Cr(CO)_6^+$ with Xe. *J. Chem. Phys.* **123**:154311/1–9.
- Meroueh O, Hase WL (1999): Collisional activation of small peptides. *J. Phys. Chem. A* **103**:3981–3990.
- Meroueh O, Hase WL (2000): Energy transfer pathways in the collisional activation of peptides. *Int. J. Mass Spectrom.* **201**:233–244.

- Meroueh O, Hase WL (2001): Effect of surface stiffness on the efficiency of surface-induced dissociation. *Phys. Chem. Chem. Phys.* **3**:2306–2314.
- Meroueh O, Hase WL (2002): Dynamics of energy transfer in peptide-surface collisions. *J. Am. Chem. Soc.* **124**:1524–1531.
- Meroueh SO, Wang Y, Hase WL (2002): Direct dynamics simulations of collision- and surface-induced dissociation of N-protonated glycine. Shattering fragmentation. *J. Phys. Chem. A* **106**:9983–9992.
- Miller SA, Luo H, Pachuta S, Cooks RG (1997): Soft-landing of polyatomic ions at fluorinated self-assembled monolayer surfaces. *Science* **275**:1447–1450.
- Morris MR, Riederer Jr DE, Winger BE, Cooks RG, Ast T, Chidsey CED (1992): Ion/surface collisions at functionalized self-assembled monolayer surfaces. *Int. J. Mass Spectrom. Ion Proc.* **122**:181–217.
- Paizs B, Suhai S (2001): Theoretical study of the main fragmentation pathways for protonated glycylglycine. *Rapid Commun. Mass Spectrom.* **15**:651–663.
- Peslherbe GH, Wang H, Hase WL (1999): Monte Carlo sampling for classical trajectory simulations. *Adv. Chem. Phys.* **105**:171–202.
- Pettersson LGM, Bauschlicher, Jr. CW, Halicioglu T (1987): Small Al clusters. II. Structures and binding in Al_n ($n = 2-6, 13$). *J. Chem. Phys.* **87**:2205–2213.
- Rahaman A, Zhou JB, Hase WL (2006): Effect of projectile orientation and surface impact site on the efficiency of projectile excitation in surface-induced dissociation. Protonated diglycine collisions with diamond {111}. *Int. J. Mass Spectrom.* **249–250**:321–329.
- Raz T, Levine RD (1996): On the shattering of clusters by surface impact heating. *J. Chem. Phys.* **105**:8097–8102.
- Schlick T (2002): *Molecular Modeling and Simulation*, Springer, New York.
- Schultz DG, Weinhaus SB, Hanley L, de Sainte Claire P, Hase WL (1997): Classical dynamics simulations of $SiMe_3^+$ ion surface scattering. *J. Chem. Phys.* **107**:9677–9686.
- Shin HK (1976): Vibrational energy transfer. In Miller WH (ed), *Dynamics of Molecular Collisions*, Part A, Plenum Press, New York, pp. 131–210.
- Sloane CS, Hase WL (1977): On the dynamics of state selected unimolecular reactions. Chloroacetylene dissociation and predissociation. *J. Chem. Phys.* **66**:1523–1533.
- Smith DL, Wysocki VH, Colorado Jr. R, Shmakova OE, Graupe M, Lee TR (2002): Low-energy ion-surface collisions characterize alky- and fluoroalkyl-terminated self-assembled monolayers on gold. *Langmuir* **18**:3895–3902.
- Smith DL, Selvan R, Wysocki VH (2003): Reactive ion scattering spectrometry of mixed methyl- and hydroxy-terminated alkanethiolate self-assembled monolayers. *Langmuir* **19**:7302–7306.
- Song K, de Sainte Claire P, Hase WL, Hass KC (1995): Comparison of molecular dynamics and variational transition state theory calculations of the rate constant for H-atom association with the diamond {111} surface. *Phys. Rev. B* **52**:2949–2958.
- Song K, Meroueh O, Hase WL (2003): Dynamics of $Cr(CO)_6^+$ collisions with hydrogenated surfaces. *J. Chem. Phys.* **118**:2893–2902.
- Stewart JJP (1989): Optimization of parameters for semiempirical methods. *J. Comput. Chem.* **10**:209–220.
- Su C-X, Armentrout PB (1993): Collision-induced dissociation of Cr_n^+ ($n = 2-21$) with Xe: Bond energies, dissociation pathways and structures. *J. Chem. Phys.* **99**:6506–6516.

- Sun L, Hase WL (2003): Born-Oppenheimer direct dynamics classical trajectory simulations. In Lipkowitz KB, Larter R, Cundari TR (eds), *Reviews in Computational Chemistry*, Vol. 19, Wiley-VCH, Hoboken, NJ, pp. 79–146.
- Truhlar DG, Muckerman JT (1979): Reactive scattering cross sections III. Quasiclassical and semiclassical methods. In Bernstein RB (ed), *Atom-Molecule Collision Theory*, Plenum, New York, pp. 505–566.
- Wang J, Meroueh SO, Wang Y, Hase WL (2003a): Efficiency of energy transfer in protonated diglycine and dialanine SID. Effects of collision angle, peptide ion size, and intramolecular potential. *Int. J. Mass Spectrom.* **230**:57–64.
- Wang Y, Hase WL, Song K (2003b): Direct dynamics study of N-protonated diglycine surface-induced dissociation. Influence of collision energy. *J. Am. Soc. Mass Spectrom.* **14**: 1402–1412.
- Whyte AR, Lim KF, Gilbert RG, Hase WL (1988): The calculation and interpretation of average collisional energy transfer parameters. *Chem. Phys. Lett.* **152**:377–381.
- Wilson Jr. EB, Decius JC, Cross PC (1955): *Molecular Vibrations*, McGraw-Hill, New York.
- Yalcin T, Khouw C, Csizmadia IG, Peterson MR, Harrison AG (1995): Why are B ions stable species in peptide spectra? *J. Am. Chem. Soc. Mass Spectrom.* **6**:1165–1174.
- Yan TY, Hase WL (2002): Comparison of models for simulating energy transfer in Ne-atom collisions with an alkyl thiolate self-assembled monolayer. *J. Phys. Chem. B* **106**: 8029–8037.
- Yardley JT (1980): *Introduction to Molecular Energy Transfer*, Academic Press, London, pp. 95–129.